# Advanced Design of Metal Nanoclusters and Single Atoms Embedded in C 1 N 1 -Derived Carbon Materials for ORR, HER, and OER

Javier Quílez-Bermejo, Sergio García-Dalí, Ayoub Daouli, Andrea Zitolo, Rafael L.S. Canevesi, Mélanie Emo, María T. Izquierdo, Michael Badawi, Alain Celzard, Vanessa Fierro

# Advanced Design of Metal Nanoclusters and Single Atoms Embedded in $C_1N_1$-derived Carbon Materials for ORR, HER and OER

*Javier Quílez-Bermejo*[1,2,*], *Sergio García-Dalí*[1,3], *Ayoub Daouli*[4], *Andrea Zitolo*[5], *Rafael Canevesi*[1], *Mélanie Emo*[6], *María T. Izquierdo*[7], *Michael Badawi*[4], *Alain Celzard*[1,8], *Vanessa Fierro*[1,*]

[1]Université de Lorraine, Centre National de la Recherche Scientifique (CNRS), Institut Jean Lamour (IJL), F-88000, Épinal, France.

[2]Departamento de Química Inorgánica and Instituto de Materiales, Universidad de Alicante, Ap. 99, 03080, Spain.

[3]Departamento de Ciencia de los Materiales e Ingenieria Metalúrgica, Universidad de Oviedo, 33004, Oviedo, Spain.

[4]Laboratoire de Physique et Chimie Théoriques (LPCT), UMR 7019 CNRS, Université de Lorraine, F-54000 Nancy, France

[5]Synchrotron SOLEIL, L'orme des Merisiers, BP 48 Saint Aubin, Gif-sur-Yvette, France.

[6]Université de Lorraine, Centre national de la Recherche Scientifique (CNRS), Institut Jean Lamour (IJL), 54011 Nancy, France

[7]Instituto de Carboquímica (ICB-CSIC), Miguel Luesma Castán 4, E-50018, Zaragoza, Spain.

[8]Institut Universitaire de France (IUF), France.

* Corresponding authors:
E-mail address: javier.quilez-bermejo@univ-lorraine.fr (Javier Quílez-Bermejo )
vanessa.fierro@univ-lorraine.fr (Vanessa Fierro)

**Keywords**: $C_1N_1$; Metal Nanoclusters; Single Atoms; Electrocatalysts; Carbon Materials

**Abstract:** Single atoms and nanoclusters of Fe, Ni, Co, Cu and Mn were systematically designed and embedded in a well-defined $C_1N_1$-type material that has internal cavities of

about 0.6 nm based on four N atoms. These N atoms serve as perfect anchoring points for the nucleation of small nanoclusters of different metal natures through the creation of metal-nitrogen (TM-$N_4$) bonds. After pyrolysis at 800 °C, TM@$CN_x$-type structures were obtained, where TM is the transition metal and $x < 1$. Fe@$CN_x$ and Co@$CN_x$ were the most promising for ORR and HER, respectively, with a Pt-like performance, and Ni@$CN_x$ was the most active for OER with an $E_{OER}$ of 1.59 V vs RHE, far outperforming the commercial $IrO_2$ ($E_{OER}$ = 1.72 V). This systematic and benchmarking study can serve as a basis for the future design of advanced multi-functional electrocatalysts by modulating and combining the metallic nature of nanoclusters and single atoms.

## 1. Introduction

The increase in global energy demand has led to considerable efforts by the scientific community to reduce the environmental issues associated with our economic system's dependence on fossil fuels [1,2]. Fuel cells and metal-air batteries, for example, have emerged as the most promising green technologies to replace conventional devices based on fossil fuels, especially using hydrogen produced by water electrolysis [3–5]. Electrochemistry is at the core of all these technologies, with electrochemical reactions requiring the presence of electrocatalysts to enhance their sluggish kinetics [6]. The oxygen reduction reaction (ORR), oxygen evolution reaction (OER) and hydrogen evolution reaction (HER) are bottlenecks in the development of green energy systems [7–9]. The limited availability and exorbitant cost of the benchmark electrocatalysts (i- platinum nanoparticles supported on carbon black for ORR and HER, and ii- $IrO_2$ or $RuO_2$-based compounds for OER) have forced scientific efforts to focus on the development of low-cost electrodes.

Non-precious metal catalysts are proposed as highly efficient and low-cost alternatives to these precious metal-containing electrodes [10]. This is especially noteworthy when using metal nanoclusters (MNs) or single-atom catalysts (SACs), since decreasing the size of the

active metal to nanoclusters or single atoms leads to almost complete exposure of the active sites and thus to superior atomic utilization and outstanding electronic properties [11]. The development of MNs and SACs has emerged as a new branch of materials science in recent years, showing superb performance for multiple applications. In electrocatalysis, atomic-scale metal conformations have also shown to be promising alternative electrodes by outperforming the catalytic activity of conventional catalysts [12,13]. Isolated transition metals (TMs) in the form of MNs and SACs have shown excellent catalytic properties for ORR, OER or HER [14–16]. However, all these metals have been evaluated individually in different carbon supports, making it impossible to predict which transition metal is the most desirable to explore in order to design advanced electrocatalysts for ORR, OER and HER.

Inspired by the enhanced properties of TM-based nanoclusters and the lack of comparative information, we systematically designed and embedded isolated TM single atoms and nanoclusters in a 2D carbon structure derived from $C_1N_1$. Compared to other carbon precursors, $C_1N_1$ appears to be a promising well-defined carbon precursor because of the multiple internal cavities based on edge-type N-containing atoms that serve as nucleation points for the formation of tailored TM-$N_4$ single atoms or nanoclusters. The resulting materials, obtained by pyrolysis of the TM-doped $C_1N_1$ precursors, lead to materials of the general formula TM@$CN_x$, where $x < 1$ due to the evolution of part of the nitrogen during the heat treatment. These materials were then extensively studied by state-of-the-art characterization techniques and their catalytic properties were examined and compared for ORR, OER and HER. The systematic analysis provides further insights for the future design of highly active multifunctional electrocatalysts in which the selected metal appears to play a primary role in the catalytic activity towards these three reactions.

## 2. Results and Discussion

### 2.1. Physicochemical characterization

Figure 1a schematically illustrates the synthesis strategy of TM@$CN_x$ materials. First, $C_1N_1$ was obtained according to the protocol described elsewhere [17,18]. $C_1N_1$ material was synthesized using guanine heat-treated at 700 °C under nitrogen atmosphere. The yield of heat treatment of guanine to obtain $C_1N_1$ was 20 %, in agreement with previous TGA experiments of guanine in nitrogen atmosphere [17,18]. The $C_1N_1$-like structure is characterized by the presence of internal cavities of about 0.6 nm [19] that can serve as an ideal anchoring point by providing multiple interactions with nitrogen atoms, themselves acting as nucleation points for the subsequent growth of small TM-based MNs. The pristine 2D structure of $C_1N_1$ and the homogeneous distribution of carbon and nitrogen atoms are confirmed by TEM images (Figure S1a) and EDX mapping (Figure S1b-d), respectively. Moreover, the C/N ratio was determined to be 1.3 (Table S1), which is in agreement with previous studies [17,18]. Subsequently, in order to introduce TM atoms into the carbon structure, the generated $C_1N_1$ was mixed with Fe, Co, Cu, Ni or Mn chloride by mechanosynthesis using a ball-milling equipment. The resulting mixture was heat-treated at 800 °C to obtain small TM-based nanoclusters embedded in a carbon material derived from $C_1N_1$, denoted as TM@$CN_x$ where TM is either Fe, Co, Cu, Ni or Mn and where x is the C/N atomic ratio of the resulting material. Table S1 shows the composition of the TM@$CN_x$ materials. The C/N ratio significantly increases as a result of gasification of the pristine $C_1N_1$ material at 800 ºC in the presence of metals, which mainly produces N evolution, resulting in the increase of the C/N ratio and the formation of TM-$N_4$ single atoms.

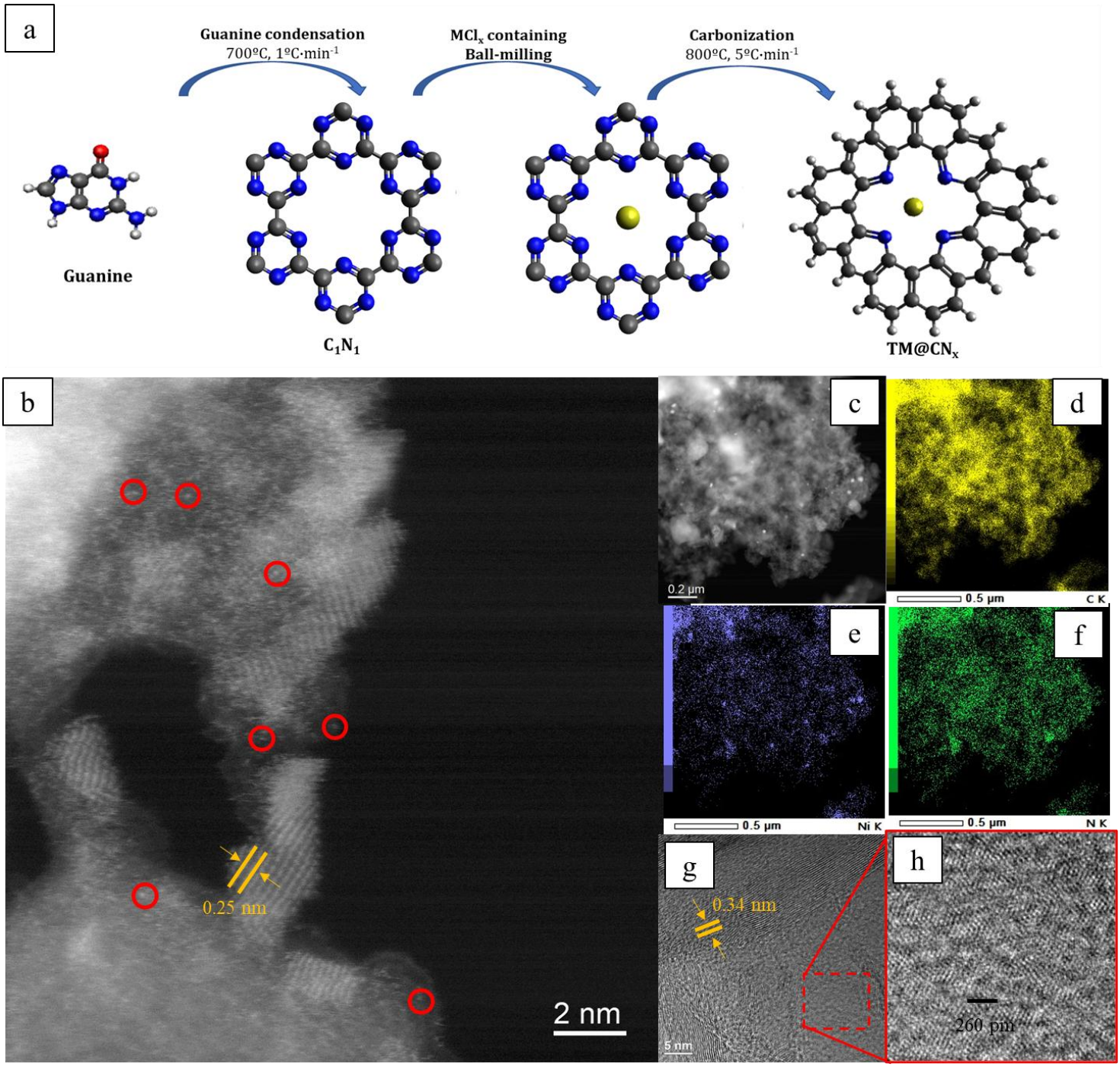


Figure 1 : (a) Schematic illustration of the experimental synthesis of TM@$CN_x$ materials. (b) High magnification HAADF-STEM image of Ni@$CN_x$, where the red circles highlight single atom disposition of Ni. (c) Low-magnification TEM image of Ni@$CN_x$, and (d-f) corresponding EDX mapping of carbon, nickel and nitrogen, respectively. (g) High-resolution TEM images of Ni@$CN_x$ in a nickel-free region. (h) FFM of the red box in Figure 1g, where the graphene-like structure is observed.

High-resolution transmission electron microscopy (HRTEM) and high-angle annular dark-field scanning transmission electron microscopy (HAADF-STEM) images of the TM@$CN_x$ samples reveal the successful introduction of small metallic nanoclusters, in which the atomic

arrangement with an interplanar distance of 0.25 nm is clearly observed for the Ni@$CN_x$ material (Figure 1b). Similar nanoclusters were also obtained for all TM@$CN_x$ materials (see Figure S2-S4), except for Cu@$CN_x$, which does not show the presence of nanoclusters but only single atoms (Figure S5a). Moreover, a large contribution of bigger nanoparticles (≈ 50 nm in diameter) was also detected in Fe@$CN_x$ (Figure S3). This confirms that the $C_1N_1$ serves as an excellent N-containing carbon precursor for the preparation of metallic single atoms and nanoclusters embedded in an N-doped carbon material, regardless of the TM employed in the synthesis. Here it is worth noting that the nature of the doping metal seems to influence slightly the resulting structure of the TM nanoclusters and C/N ratio. Nevertheless, single atoms were detected in the 2D $C_1N_1$-derived carbon structure using all metal precursors (red circles in Figure 1b for Ni@$CN_x$ and Figures S2-S5 for Co@$CN_x$, Fe@$CN_x$, Mn@$CN_x$ and Cu@$CN_x$, respectively). In addition, energy-dispersive X-ray spectroscopy (EDX) mapping images confirm the homogeneous and uniform distribution of nitrogen species and metal nanoclusters over the carbon skeleton (Figure 1c-f for Ni@$CN_x$ and Figures S2-S5 for the other TM@$CN_x$ materials). Figure 1g shows that the addition of single atoms or metal nanoclusters in the $C_1N_1$-type structure does not affect the 2D properties of the carbon material, exhibiting a lamellar nanostructure with a 0.34 nm interlayer distance, characteristic of graphene-like structures that also work as a core shell for TM nanoparticles [20]. Moreover, the Fast Fourier Transform (FFT, Figure 1h) of the bright-field images show well-ordered atomic structures in the graphenic layers.

The textural properties of the materials were studied by $N_2$ adsorption-desorption isotherms at -196 °C (Figure S6a) and are summarized in Table S1. The Pore Size Distribution (PSD) of the pristine $C_1N_1$ (Figure S6) demonstrates the presence of a high contribution of ultramicropores with a pore size diameter of 0.5-0.8 nm, which confirms the development of defined internal cavities characteristic of the $C_1N_1$ material. These pores can expose a large

amount of TM-$N_4$ active sites for further nucleation, as confirmed by HAADF images. After the introduction of the metal nanoclusters and the second heat treatment, the PSDs of the TM@$CN_x$ materials show a significant decrease in the contribution of this peak since most of them are now blocked by the presence of the metal nanoclusters (Figures 2a and 2b). Moreover, the pyrolysis also led to condensation reactions of the carbon layers that favored the carbon enrichment of the pristine $C_1N_1$. A slight mesoporous contribution was also observed for the TM@$CN_x$ samples. NLDFT surface areas of 210-330 $m^2$ $g^{-1}$ were observed for all materials (Table S1). This confirms that the internal cavities of $C_1N_1$ have served as

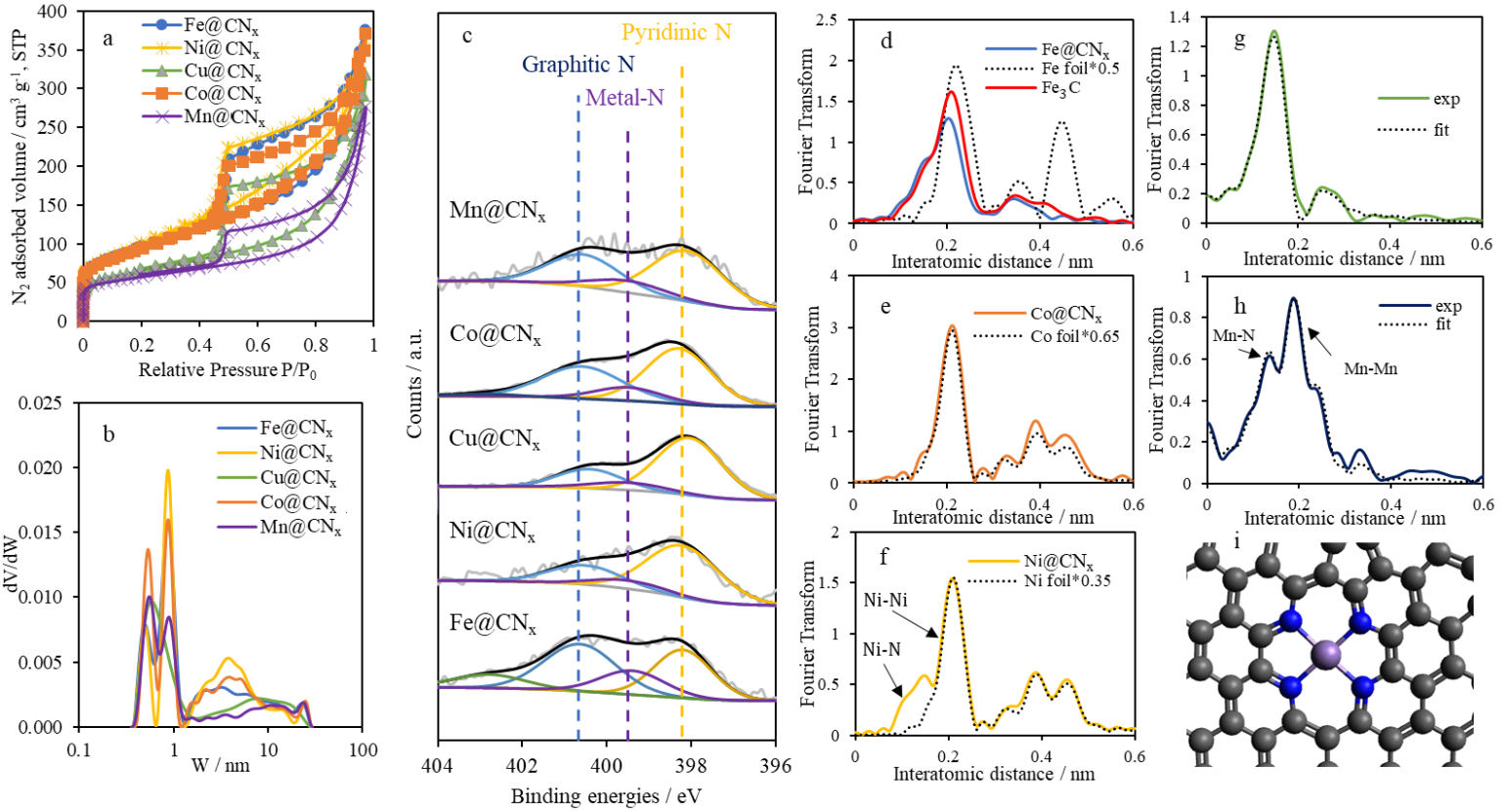


excellent sites for anchoring TM-$N_4$ single atoms and nanoclusters while maintaining the textural properties of the pristine material.

Figure 2: (a) $N_2$ adsorption isotherms at -196 °C, (b) pore size distributions and (c) N1s spectra of TM@$CN_x$ materials. V represents the volume of adsorbed nitrogen and W represents the pore width in the pore size distributions. N1s spectra show three main peaks that are related to the presence of pyridinic N (yellow), metal-N species (violet) and graphitic N (blue). Non-phase shift corrected FT-EXAFS spectra of (d) Fe@$CN_x$ and metallic Fe foil (intensity multiplied by a factor of 0.50) and $Fe_3C$ as references, (e) Co@$CN_x$ and metallic Co foil reference (intensity multiplied by a factor 0.65), (f) Ni@$CN_x$ and metallic Ni foil reference (intensity multiplied by a factor 0.35). EXAFS analysis of the metal K edge in the Fourier transformed space of (g) Cu@$CN_x$ and (h) Mn@$CN_x$. The black curves represent the calculated spectra, while the green and

violet curves represent the experimental spectra at the K edge of Cu and Mn, respectively. (i) Schematic illustration of TM-$N_4$ species (Mn in violet, N in blue, and C in grey).

X-Ray photoelectron spectroscopy (XPS) was used to characterize the surface chemistry of the TM@$CN_x$ materials. The high-resolution N1s spectra were deconvoluted into three peaks related to the presence of pyridinic N (398.2 ± 0.2 eV), metal-N (M-N) species (399.5 ± 0.2 eV) and graphitic N (401.2 ± 0.2 eV) [21–23] for all TM@$CN_x$ materials (Figure 2c). The clear contribution of the M-N peak located at 399.5 eV demonstrates the presence of TM-$N_4$ coordination sites. The Fe2p, Ni2p, Cu2p, Co2p and Mn2p spectra of Fe@$CN_x$, Ni@$CN_x$, Cu@$CN_x$, Co@$CN_x$ and Mn@$CN_x$, respectively, reveal the positively charged oxidation state of the metal species (Figure S7), which indicates that the metal atoms in the nanoclusters are mainly coordinated with the N heteroatoms in the carbon skeleton. Nevertheless, the presence of oxidized metallic species cannot be discarded, since the peak related to M-O species appears at similar binding energies.

X-ray absorption spectroscopy (XAS) was used to investigate accurately the nature and local structure of metal species present in the TM@$CN_x$ catalysts. Figure 2d shows that the Fourier transform (FT) of the extended X-ray absorption fine structure (EXAFS) spectrum of Fe@$CN_x$ is characterized by a first-shell peak at about 0.204 nm, which is located in the Fe-Fe backscattering peak of the $Fe_3C$ reference. The identification of an iron carbide phase, and not pure Fe nanoparticles, is even clearer if one observes the correspondence between the imaginary part of the FT-EXAFS signals of Fe@$CN_x$ and $Fe_3C$, as these signals are very sensitive to the bond length of the absorber-scatterer pair (Figure S8). The Fe K-edge X-ray absorption near edge spectroscopy (XANES) spectrum of Fe@$CN_x$ shows a positive shift of the absorption threshold compared to the reference $Fe_3C$ spectrum (Figure S9), consistent with the presence of an iron fraction in a higher oxidation state and coordinated by light atoms (C, N, or O). According to the presence of single atoms in HAADF-STEM images, this higher oxidation state appears to be related to the presence of Fe-$N_4$ species throughout the carbon

framework. The FT-EXAFS spectrum of Co@$CN_x$ matches well with the spectrum of the reference metallic Co (Figure 2e), in agreement with the HRTEM images revealing the presence of core-shell nanoclusters (Figure S2f). However, while the Co K-edge XANES spectra of Co@$CN_x$ and crystalline Co show similar spectral features, the higher absorption at about 7728 eV in the XANES spectrum of Co@$CN_x$ is indicative of a fraction of Co atoms in a higher oxidation state than the metallic one (Figure S10). This perfectly matches the presence of small nanoclusters (see again HAADF-STEM images in Figure S2), in which a portion of the Co atoms are coordinated to light atoms in the carbon material. The FT-EXAFS spectral features of Ni@$CN_x$ are in excellent agreement with the Ni-Ni backscattering of crystalline Ni at 0.209 nm, while the peak around 0.148 nm is assigned to the coordination between Ni and N (or a light atom like C, O) in Ni-$N_4$ moieties (Figure 2f). Interestingly, a linear combination fit of the Ni K-edge XANES spectrum of Ni@$CN_x$, using the Ni foil and a single-atom Ni NC catalyst derived from ZIF-8 [24] as reference spectra, allowed us to estimate the contents of Ni metal nanoparticles and Ni SAC to be 41% and 59%, respectively (Figure S11). Fitting the EXAFs spectrum of Cu@$CN_x$ reveals the presence of about 4 N atoms at 0.195 nm coordinated to the Cu center, in agreement with a Cu-$N_4$ moiety embedded in the graphitic matrix [25], while the absence of a Cu-Cu backscattering at 0.215 nm confirms the single-metal atom nature of the active sites (Figure 2g and Table S2). Regarding Mn@$CN_x$, the EXAFS analysis allowed us to identify the nature of the peak at 0.188 nm as a Mn-Mn backscattering from a Mn carbide phase (Figure 2h). Indeed, the position of this peak does not correspond to the signal of crystalline Mn, and the EXAFS distance of 0.223 nm is consistent with the Mn-Mn bond distance in $Mn_3C$ [26]. The peak at 0.136 nm is correctly reproduced by the geometry of a Mn-$N_4$ moiety enclosed in a graphene plane (Figure 2i). The structural parameters of the fitting procedure are reported in Table S2.

## 2.2. Electrocatalytic performance

The electrochemical performance towards ORR, HER and OER was evaluated in a three-electrode cell with a rotating ring-disk electrode (RRDE). Commercial benchmark catalysts (Pt/C and $IrO_2$) were included for comparison when discussing the catalytic results.

### *2.2.1. Oxygen reduction reaction (ORR)*

The electrocatalytic activity of the TM@$CN_x$ materials towards the ORR was evaluated in both $O_2$-saturated alkaline (0.1 M KOH) and acidic (0.5 M $H_2SO_4$) electrolytes by linear sweep voltammetry (LSV). Figure 3 shows the LSV curves of all materials in 0.1 M KOH solution. Fe@$CN_x$ and Mn@$CN_x$ show an outstanding onset potential ($E_{ONSET}$) of 0.94 V and a half-wave potential ($E_{1/2}$) of 0.84 V, better than the samples Co@$CN_x$ (0.92 V and 0.79 V, respectively), Cu@$CN_x$ (0.90 V and 0.79 V, respectively) and Ni@$CN_x$ (0.85 V and 0.74 V, respectively). In the case of Fe@$CN_x$, its highly efficient catalytic activity towards the ORR can be associated with the presence of $FeN_4$ sites, as reported in the literature [27,28]. Nevertheless, the contribution of $Fe_3C$ nanoparticles in the materials has been shown to be responsible for an increase in the electron density of the iron atom in the $FeN_4$ species, leading to improved ORR performance [29]. Similar synergistic effect can explain the high catalytic performance in Mn@$CN_x$, where the catalytic activity of $MnN_4$ species has been proven [30]. Nevertheless, the origin of the catalytic activity when comparing single-atoms and nanoclusters requires deeper research. To verify further the role of TM in ORR catalytic activity, the pristine $C_1N_1$ was evaluated as electrocatalysts since quaternary nitrogen species were also found to be active for the ORR [31,32]. Figure S12 shows the poor catalytic activity of $C_1N_1$ compared to Fe@$CN_x$ and Mn@$CN_x$, revealing the crucial role of metal nanoclusters and single atoms embedded in the $C_1N_1$-derived carbon structure. Furthermore, the heat treatment temperature for the most catalytic TM@$CN_x$ material was optimized. Figure S12

shows the catalytic activity of Fe@$CN_x$ obtained at different temperatures (from 700 to 900 ºC). A maximum of catalytic activity seems to be reached in the range of 800-900 ºC, while the catalysts prepared at temperatures lower than 700 ºC show lower catalytic performance for ORR. Although the nature of the metal seems to play an important role in ORR activities, all transition metals show high catalytic properties towards the ORR, with Ni@$CN_x$ being the only material to exhibit poor catalytic performance. The high activity is particularly notable in the Fe- and Mn-based materials, which exceed the catalytic activity of commercial platinum-based electrode in terms of $E_{1/2}$ value (see Figure S13). The number of electrons transferred during the ORR is a primary value to assess the mechanisms driving the reaction, depending on the material. The number of electrons transferred varies in the opposite direction of the amount of hydrogen peroxide produced (Figure 3b). High $H_2O_2$ production means a loss of energy efficiency towards power generation as well as increased corrosion potential. $H_2O_2$ yields of less than 10% were found in Fe and Mn materials, while Cu, Co and Ni showed $H_2O_2$ yields of 20-40 % in the 0.0 - 0.7 V range. Therefore, in agreement with the obtained results, the most catalytic nanoclusters with high selectivity towards the 4-electron pathway follow the order: Mn ≈ Fe > Co > Cu > Ni for the alkaline ORR (Figure S14).

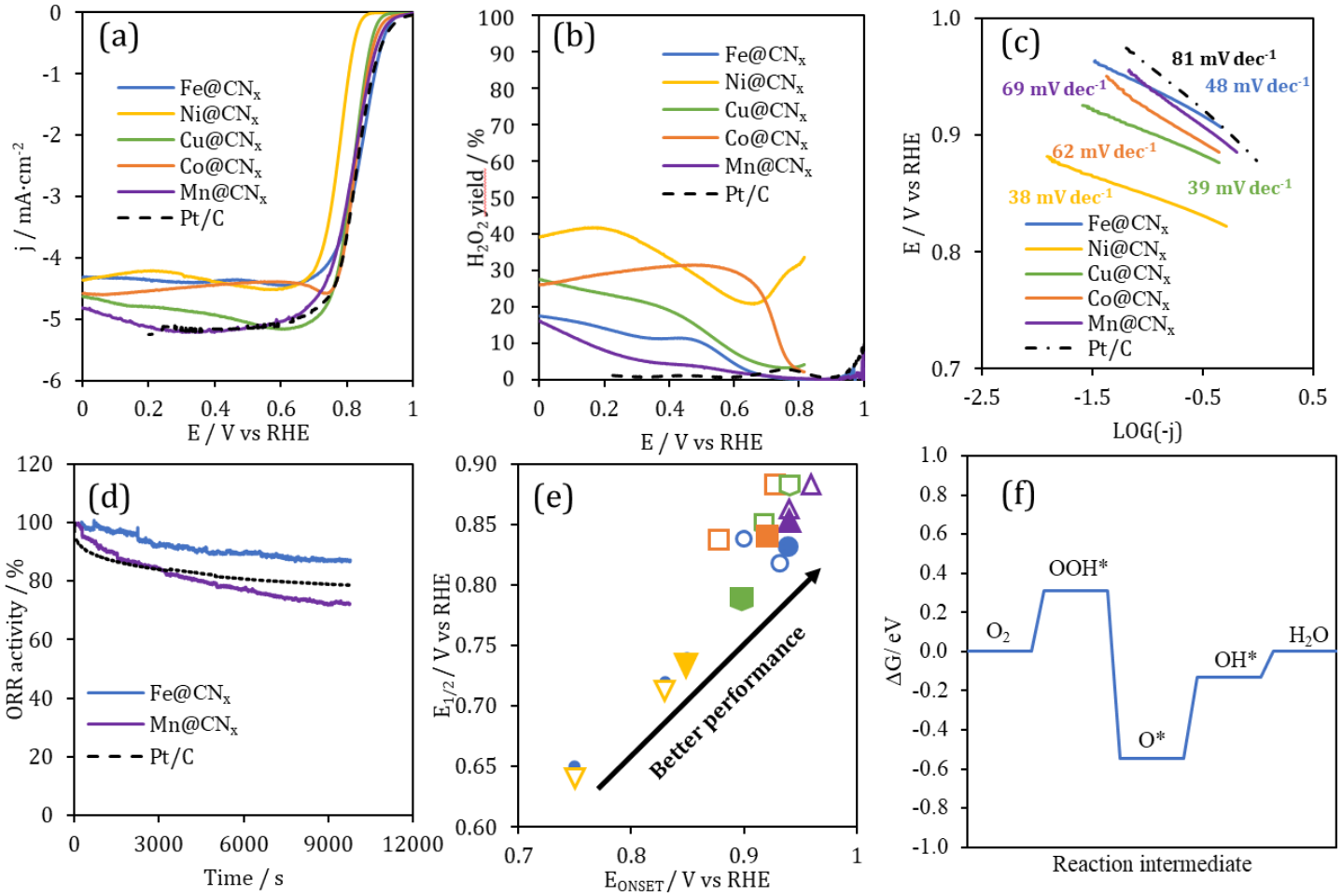


Figure 3: (a) LSV curves, and (b) $H_2O_2$ yield of TM@$CN_x$ samples in $O_2$-saturated 0.1 M KOH solution at a scan rate of 5 mV·$s^{-1}$ and 1600 rpm, compared to Pt/C. (c) Tafel slopes obtained from the kinetic potential range in the LSV curves during ORR measurements. (d) Chronoamperometric analysis at a fixed potential of 0.65 V vs RHE for Mn@$CN_x$, Fe@$CN_x$ and Pt/C catalysts. (e) Comparison of performance of our catalysts with other TM-based electrocatalysts available in the open literature for ORR in 0.1 M KOH. Blue circles, yellow inverted triangles, orange squares, green pentagons and violet triangles represent Fe-, Ni-, Co-, Cu- and Mn-based catalysts, respectively. The solid symbols correspond to the data obtained in this work. (f) ORR free energy diagram using $FeN_4$ cluster as model electrocatalyst.

The ORR kinetics were determined from Tafel slopes (Figure 3c) and indicate that the commercial Pt/C catalyst (87 mV·$dec^{-1}$) has the worst kinetics towards the ORR compared to the TM@$CN_x$ materials (from 38 to 69 mV·$dec^{-1}$). Furthermore, the durability of the most catalytic TM@$CN_x$ materials was tested by chronoamperometric analysis at a fixed potential, 0.65 V vs RHE. As shown in Figure 3e, the Faradaic retention of catalytic activity for the Fe@$CN_x$ and Mn@$CN_x$ samples was 86 and 73 % after 10,000 s, respectively. Moreover, the CV after the stability test of the Fe@$CN_x$ sample shows a similar profile to the CV before the chronoamperometric test (Figure S15), which supports the high stability of the material under the working conditions. Although they exhibit similar catalytic activities, the large differences

in the chronoamperometric analysis of the two materials highlight the greater stability of the Fe moieties, consistent with the robustness of Fe-$N_4$ species [33]. Moreover, the Fe@$CN_x$ material shows significantly higher stability than the commercial Pt/C (76%), indicating that this material is a promising electrocatalyst to replace commercial Pt-based electrodes in alkaline electrolyte. Table S3 puts the high catalytic activity and selectivity of TM@$CN_x$ materials for ORR into perspective by comparing them to the best electrocatalysts in the recent literature [34,35,44,36–43]. Figure 3f schematizes the comparisons gathered in Table S3, clearly showing that the nature of the metal atom seems to be determinant in the catalytic activity towards the ORR. In the literature, as in our systematic study, Mn is the most active TM, showing the best $E_{ONSET}$ and $E_{1/2}$, closely followed by Fe, Co and Cu. At the same time, Ni SACs show poor performance towards the ORR with the lowest values reported in the open literature.

Moreover, the electrocatalytic ORR performance of TM@$CN_x$ materials was also studied in a 0.5 M $H_2SO_4$ acidic solution. As shown in Figure S16, the ORR activity of the materials is significantly lower in an acidic electrolyte than in an alkaline electrolyte. It is widely known that electrocatalysts show a higher overpotential towards the ORR in an acidic electrolyte because of the interaction of $H_3O^+$ cations with reaction intermediates that limit the completion of the ORR [45,46]. Mn@$CN_x$ also appears to be the most promising TM@$CN_x$ electrocatalysts for acidic ORR, with higher $E_{ONSET}$ and half-wave potential, followed by Co@$CN_x$ and Fe@$CN_x$. Again, the catalytic activities of Cu@$CN_x$ and Ni@CNx are far from the best activities. The number of electrons transferred and $H_2O_2$ yield in acidic solution confirm a high selectivity towards 4-electron mechanism for all materials, as all TM@$CN_x$ materials show $H_2O_2$ yield below 20%, although there are slight differences depending on the potential.

In order to explain the high catalytic activity of Fe@$CN_x$, Density Functional Theory (DFT) theory was used to further understand the ORR mechanisms, using Nørskov's approach [47], as described in the experimental section (Tables S6 and S7). To model the catalytic site, we considered a single Fe atom linked to 4 nitrogen atoms (in line with XPS, HAADF, and XAS experiments), embedded in a graphene-like structure (see Figure S17 and computational details). As the $O_2$ chemisorption step is of paramount importance when investigating the ORR activity, different molecular orientations of $O_2$ (side-on and end-on) along with three possible iron spin states were computed and depicted in Table S7 (see also Supporting Information for details). The end-on triplet configuration (Figure S17) with an $O_2$ binding energy of -1.63 eV was found to be the most stable ground state. Subsequently, Figure 3f shows the free energy diagram corresponding to the different ORR steps over $FeN_4$ cluster at 1.23 V. As observed, the most endergonic step is the third reduction stage, which is related to the first water desorption ($\Delta G_{OH^*}$ = 0.41 eV). The O* configuration (Figure S17) is the most stable intermediate, and higher energy requirements are necessary to continue with the subsequent reduction steps. Nevertheless, from a thermodynamic point of view, only 0.41 eV is required to proceed with the introduction of the next electron-proton pair, which is low compared to other single atoms and supports the high catalytic activity of $FeN_4$ sites[48].

*2.2.2. Hydrogen evolution reaction (HER)*

The electrocatalytic activity towards HER was also examined in alkaline (1.0 M KOH) and acidic (0.5 M $H_2SO_4$) solutions. In the case of HER, the descriptor to evaluate the catalytic activity is the potential required to reach -10 $mA \cdot cm^{-2}$ ($E_{HER}$). As shown in Figure 4, the most efficient TM@$CN_x$ was obtained after the introduction of Co nanoclusters. Co@$CN_x$ shows outstanding properties towards HER, with $E_{HER}$ = -0.27 V in alkaline solution and $E_{HER}$ = -0.25 V in acidic solution. The high catalytic performance of Co@$CN_x$ is related to the

presence of $CoN_x$ single atoms, as it is proven that $CoN_x$ species show similar catalytic activity in both acidic and alkaline solution, while other Co-based species, such as Co metallic nanoclusters, show pH-dependent catalytic activity for the HER [49]. Moreover, Co@$CN_x$ was prepared at different temperatures during the heat treatment with the aim of optimizing the electrocatalyst. Figure S18 shows that the most optimal catalytic activity was obtained at 800 ºC compared to Co@$CN_x$-700 and Co@$CN_x$-900 samples, reinforcing the claim that 800 ºC is the optimal temperature when using $C_1N_1$ as catalyst precursor. On the other hand, the catalytic activity of Cu@$CN_x$ is surprisingly low for the HER ($E_{HER}$ = -0.76 V vs RHE). As this material consists of single atoms only, these results indicate that single Cu atoms are not active for such an electrochemical reaction.

Regarding all TM@$CN_x$, unlike ORR, the acidic pH of the 0.5 M $H_2SO_4$ solution appears to play a positive role in HER catalysis, showing on average better performance in acidic solution than in alkaline solution. Tafel plots were calculated for all materials and provided in Figure 4b. The Tafel slopes show sluggish kinetics in the TM@$CN_x$ materials compared to the commercial Pt/C catalyst. The best kinetics in TM@$CN_x$ samples was obtained for Ni@$CN_x$ in alkaline solution with 120 mV·dec$^{-1}$, closely followed by Co@$CN_x$ with 126 mV·dec$^{-1}$. Tafel slopes of 120 mV·dec$^{-1}$ or higher are characteristic of electrocatalysts in which water adsorption (Volmer step) is the determining stage in the HER rate. In agreement with the results obtained, the most catalytic TM@$CN_x$ materials follow the order: Co > Ni > Fe > Mn > Cu for both acidic HER (Figure 4a and S19) and alkaline (Figure 4c and S20). Even though Co@$CN_x$ is still far from Pt/C in both media, Co@$CN_x$ shows excellent catalytic properties for HER, comparable to state-of-the-art TM-based electrocatalysts. In addition to the catalytic activity, the stability of this sample was tested by LSV cycling. Figure 4e shows the LSV profiles of Co@$CN_x$ before and after 100 cycles, which confirms the great stability under HER conditions by showing similar $E_{HER}$ of -0.29 V vs RHE. Furthermore,

electrochemical characterization by cyclic voltammetry of the Co@$CN_x$ sample was performed, which shows similar CV profile to that of the material before the stability test (Figure S21). This confirms the high stability of the material under the working conditions.

Table S4 and Figure 4f compare the catalytic activity of TM@$CN_x$ for HER with the most promising TM-based electrocatalysts in the recent literature[50–58]. The literature search confirms that Co and Ni-based catalysts show outstanding properties towards the HER, followed by Fe and Mn. Cu-based electrocatalysts show insufficient performance to prepare an adequate HER electrocatalyst, in agreement with our experimental results.

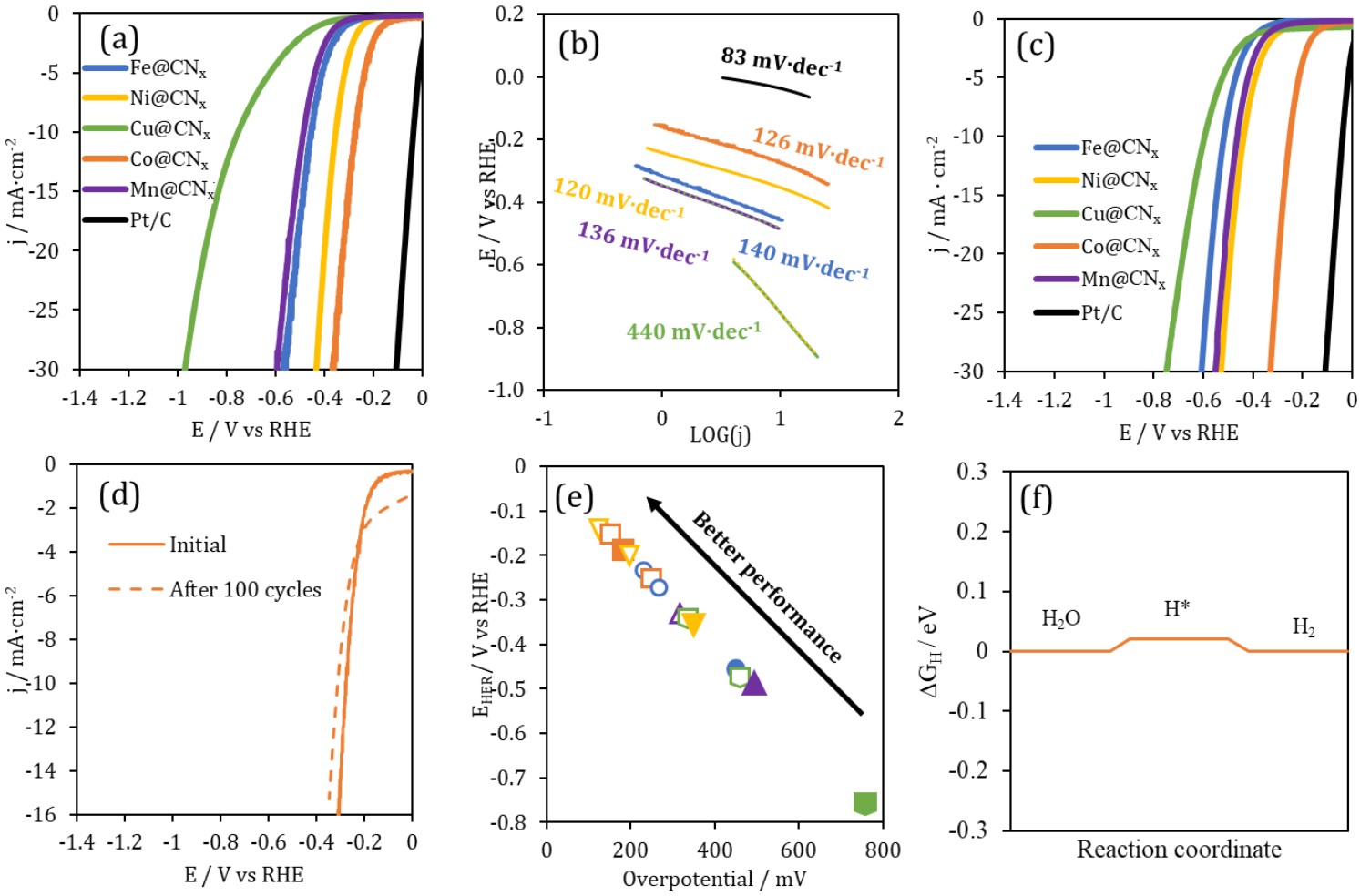


**Figure 4:** (a) LSV curves, and (b) Tafel slopes of TM@CNx samples in $N_2$-saturated 1 M KOH solution at a scan rate of 5 mV·$s^{-1}$ and 1600 rpm, compared to Pt/C. (c) LSV curves of TM@CNx samples in $N_2$-saturated 0.5 M $H_2SO_4$ solution at a scan rate of 5 mV·$s^{-1}$ and 1600 rpm. (d) LSV curves before and after 100 cycles for Co@CNx in $N_2$-saturated 0.5 M $H_2SO_4$ solution at a scan rate of 5 mV·$s^{-1}$ and 1600 rpm. (e) Literature search of transition metal-based electrocatalysts for the hydrogen evolution reaction [50–58]. Blue, yellow, orange, green and violet represent Fe-, Ni-, Co-, Cu- and Mn-based catalysts,

respectively. The solid symbols correspond to the data obtained in this work. (f) HER free energy diagram using $CoN_4$ cluster as model electrocatalyst.

Similarly to what was done for ORR, DFT modeling was performed to investigate HER mechanisms for $Co@CN_x$, based on what can be simulated for a $CoN_4$ cluster. Figure 4f shows the free energy diagram of hydrogen evolution from water and Figure S22 provides the OER intermediate configurations. The free energies of the H* intermediate are often used as a theoretical descriptor of HER performance. As observed, the low $\Delta G_{H^*}$ (0.02 eV), close to the theoretical value, is indicative of a straightforward hydrogen evolution reaction and supports the high experimental catalytic performance. Detailed intermediate HER configurations are included in the experimental section.

*2.2.3. Oxygen evolution reaction (OER)*

The catalytic activity towards the OER was examined in alkaline (1 M KOH) and acidic (0.5 $H_2SO_4$) solutions. The factor to evaluate the OER activity is often referred to as the potential required to reach 10 $mA \cdot cm^{-2}$ ($E_{OER}$). As shown in Figure 5a, $Ni@CN_x$ exhibits excellent catalytic activity towards the OER, with an $E_{OER}$ of 1.59 V vs RHE, far exceeding the benchmark $IrO_2$-based catalysts ($E_{OER}$ = 1.72 V vs RHE). The high catalytic performance of Ni-based materials may be related to $NiN_4$ species, since the electronic coupling of Ni-N bonds reduces the Fermi level and facilitates the chemisorption of OER intermediates, leading to enhanced OER on Ni- and N-doped carbon materials [59]. Nevertheless, Ni nanoclusters or nanoparticles have also proven to be highly effective towards OER [60], so both contributions may play a significant role in OER electrocatalysis. In-depth experimental and modeling research is required to better understand whether the origin of the catalytic activity in $Ni@CN_x$ comes from single-atoms or nanoclusters. The heat treatment temperature in the synthesis of $Ni@CN_x$ was optimized, and Figure S23 shows that the optimum catalytic activity was obtained with the catalyst synthesized at 800 ºC. After $Ni@CN_x$, $Fe@CN_x$ also shows superior OER activity compared to the commercial catalyst, followed by $Mn@CN_x$ and

Co@$CN_x$. Interestingly, Cu@$CN_x$ is not active in the whole potential range, indicating the weak role of Cu single atoms as active sites for OER, as for HER. The Tafel plots (Figure S24) show that, although exhibiting the best $E_{OER}$, Ni@$CN_x$ does not show the best kinetics. Fe@$CN_x$ achieved the lowest Tafel slopes of all TM@$CN_x$ materials (222 $mV \cdot dec^{-1}$), lower than those obtained with the $IrO_2$ catalyst (229 $mV \cdot dec^{-1}$). Cu@$CN_x$ shows a large Tafel slope, which is characteristic of a corrosive electrochemical reaction instead of OER. Stability experiments were performed for the best catalytic TM@$CN_x$ material and the $IrO_2$ commercial sample. In addition to the excellent OER activities, Figure 5b shows the improved stability of the Ni@$CN_x$ material after 100 OER cycles, with similar $E_{OER}$ of 1.61 V vs RHE. To further verify the high stability of the Ni@$CN_x$, CV measurements were performed after the stability test and Figure S25 shows similar CV profiles as the initial one. In agreement with the obtained results, the most catalytic TMs follow the order: Ni > Fe > Mn > Co >> Cu for alkaline OER (Figure S26). Table S5 and Figure 5c compare the catalytic activity of TM@$CN_x$ for OER with the most promising TM-based electrocatalysts from the recent open literature [35,42,58,61–66]. The trend found in this work is corroborated by the literature search, where Ni is also the most favorable metal for designing advanced OER electrocatalysts. The catalytic activity of TM@$CN_x$ materials towards OER has also been evaluated in acidic conditions (Figure S27); however, these metal nanoclusters supported on $C_1N_1$-derived carbon materials are not efficient for acidic OER. DFT modeling was also performed to better elucidate the OER mechanisms for the Ni@$CN_x$ material, based on a $NiN_4$ cluster. Figure S28 shows the elementary reaction intermediates of the HER. Figure 5d shows that the most endergonic step of the OER is the second reduction stage, which is related to the reaction $OH^* \rightarrow O^* + H^+ + e^-$ ($\Delta G = 0.95$ eV). The withdrawal of the electron-proton pair requires high energy to overcome this step. As soon as this reaction intermediate is reached, the third and fourth oxidation stages proceed easily. Consequently, an enhancement of the catalytic

activity of Ni@$CN_x$ could be achieved by overcoming the large energy requirements of the first and second oxidation stages through the use of dual- or tri-sites systems or other carbon supports, as reported elsewhere [67].

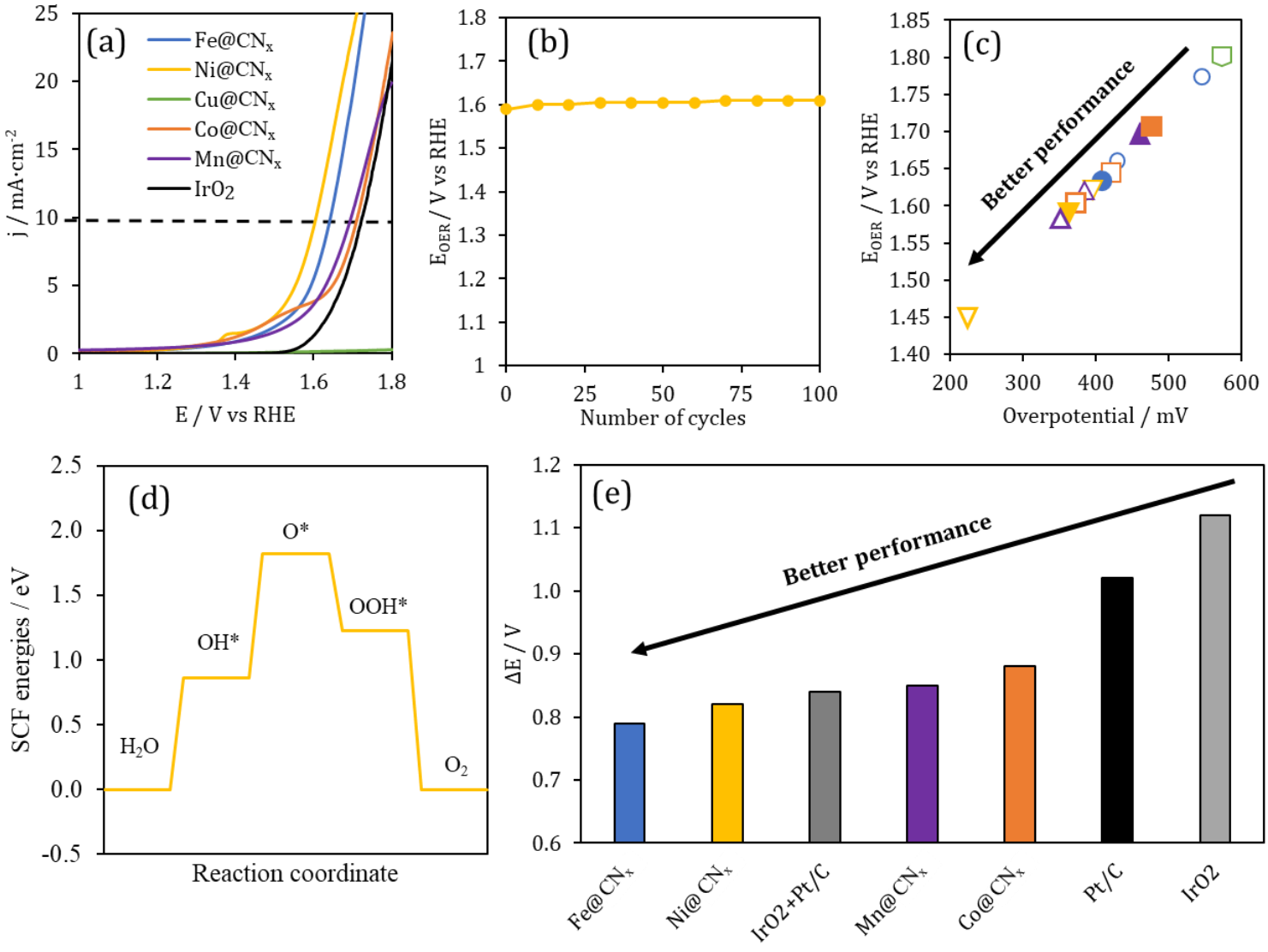


**Figure 5**: (a) LSV curves of TM@$CN_x$ materials in $N_2$-saturated 1 M KOH solution at a scan rate of 5 mV·$s^{-1}$ and 1600 rpm. (b) Representation of $E_{OER}$ vs. number of cycles during OER measurements for Ni@$CN_x$ in $N_2$-saturated 1 M KOH solution at a scan rate of 5 mv·$s^{-1}$ and 1600 rpm. (c) Literature search of transition metal-based electrocatalysts for the oxygen evolution reaction in 1.0 M KOH solution [35,42,58,61–66]. Blue, yellow, orange, green and violet represent Fe-, Ni-, Co-, Cu- and Mn-based catalysts, respectively. Cu-based catalysts found in the literature always showed $E_{OER}$ higher than 1.80 V vs RHE. The solid symbols correspond to the data obtained in this work. (d) OER free energy diagram using $NiN_4$ cluster as model electrocatalyst. (e) Bifunctional OER/ORR parameter for all TM@$CN_x$ materials. Pt/C, $IrO_2$ and their physical mixture are included for comparison.

Bifunctional ORR/OER performance is of critical interest for metal-air batteries. The oxygen electrode activity parameter, $\Delta E$ ($\Delta E = E_{OER} - E_{1/2}$), is the most commonly used descriptor to

evaluate the bifunctional properties of electrocatalysts towards ORR/OER. The smaller the oxygen electrode activity parameter, the better the bifunctional properties towards ORR/OER. The Pt/C electrocatalyst shows excellent activity towards the ORR; however, the catalysis towards the OER is very poor. At the same time, $IrO_2$ catalysts show very efficient OER activity, but larger overpotentials towards the ORR. In commercial metal-air batteries, a physical mixture of Pt/C with $IrO_2$ is thus used to achieve the best catalytic properties. As shown in Figure 5e, the bifunctional properties of TM@$CN_x$ materials were evaluated in a 1.0 M KOH solution, the results of which show better performance for Fe@$CN_x$ and Ni@$CN_x$ than the individual commercial catalysts and the physical mixture of Pt/C and $IrO_2$. Moreover, the bifunctional properties of Fe@$CN_x$ show values similar to the catalytic performance of state-of-the-art electrocatalysts.

## 3. Conclusion

This study provides an easy synthetic route to fabricate outstanding electrocatalysts and shows fundamental insights to improve the performance of ORR, OER and HER electrocatalysts. Furthermore, it paves the way for the future design of advanced bifunctional or trifunctional catalysts that could meet the industrial requirements of fuel cells, metal-air batteries, and water splitting devices. We systematically designed and fabricated single atoms and atomically distributed nanoclusters, which was confirmed by HAADF-STEM, EDX mapping, ICP, XPS and XAS, based on transition metals (TM: Fe, Ni, Cu, Co and Mn) in a $C_1N_1$-derived carbon structure. The resulting TM@$CN_x$ catalysts showed outstanding performance and stability for ORR, OER and HER. Fe@$CN_x$ is the most promising for ORR with a platinum-like performance ($E_{ONSET}$ = 0.94 V, $E_{1/2}$ = 0.84 V), Co@$CN_x$ is the most promising for HER with a $E_{HER}$ of -0.27 V, among the state-of-the-art electrocatalysts in literature and close to the commercial Pt/C electrocatalysts, and Ni@$CN_x$ is the most active for OER with a $E_{OER}$ of 1.59 V vs RHE, overperforming by far the commercial $IrO_2$ ($E_{OER}$ =

1.72 V). In addition, the findings were supported by DFT calculations, which allowed the elucidation of the different electrocatalytic mechanisms and the limiting kinetic steps. The use of the same $C_1N_1$-derived carbon support provides a unique opportunity to fairly compare the catalytic activity of the different TMs, making it possible to predict which transition metal is the most favorable for each electrochemical reaction. This comparison opens a new door to combining the most desirable transition metals in the search for catalytic activity in several electrochemical reactions.

## 4. Experimental Section/Methods

*Synthesis of TM@$CN_x$ materials:* Guanine (2.5 g, Sigma-Aldrich) was heat-treated in a high-temperature tubular furnace at 700 ºC with a heating rate of 1 ºC $min^{-1}$ under an $N_2$ flow of 150 mL $min^{-1}$. Prior to the heat treatment, the furnace was purged for 1 hour with the same flow rate at room temperature. After the heat treatment, $C_1N_1$ samples were obtained.

Then, ball-milling was used to prepare the TM@$CN_x$ materials. $C_1N_1$ (450 mg) was mixed with $FeCl_3 \cdot 6H_2O$ 750 mg). The mass of the other metal precursors was adjusted to maintain the same number of moles of metal in the mixture. Then, the mixture was ball-milled for 30 min in a planetary milling machine with agate bowl and balls (PM 100, Retsch, at a rotation speed of 500 rpm). The recovered paste was dried and subjected to a heat treatment at 800 ºC for 1 hour with a heating rate of 5 ºC $min^{-1}$. Temperatures of 700 and 900 ºC were also used to prepare the most catalytic TM@$CN_x$ materials in each electrocatalytic reaction for comparative purposes. The resultant TM@$CN_x$ was introduced into 1 M HCl (500 mL) in an ultrasonic bath for 30 min to remove excess metal that has not reacted with $C_1N_1$. Then, the materials were washed on a paper filter with 1 M HCl (1 L) and distilled water (2 L). Finally, the materials were dried in an oven at 100 ºC overnight.

*Physicochemical characterization:* Elemental analysis was used to determine carbon, nitrogen, hydrogen and oxygen contents using a Vario EL Cube analyzer (Elementar). The materials

(15 mg) were subjected to a heat treatment at 1700 ºC in an oxygen-containing helium atmosphere. The gases obtained from the combustion were then separated by a chromatographic column and analyzed by a thermal conductivity detector.

X-ray photoelectron spectroscopy (XPS) was obtained by using an ESCAPlus OMICROM spectrometer equipped with a non-monochromatized Mg·Kα X-ray source. Shyrley-type background and quantification were processed using the CASA software. Peak deconvolution of N1s and metal spectra was performed by least-square fitting using Gaussian-Lorentzian (20:80) curves.

High-resolution transmission electron microscopy (HRTEM) and scanning transmission electron microscopy (STEM) investigations were performed in a JEOL JEM_ARM 200F Cold FEG, operating at 200 kV and equipped with a spherical aberration (Cs) probe and image correctors (0.12 nm point resolution in TEM mode and 0.078 nm in STEM mode). STEM images were obtained in high-angle annular dark-field (HAADF) mode. The chemical composition was studied by energy dispersive X-ray spectroscopy (EDX), collected on a JEOL spectrometer (SDD) in STEM mode.

X-ray absorption spectroscopy (XAS) measurements were performed at the metal K-edges in transmission mode (XANES) on the SAMBA beamline of the SOLEIL synchrotron (France). The beamline is equipped with a sagittally bent double crystal Si (220) monochromator and two Pd-coated mirrors used to remove X-ray harmonics. The catalysts were pelletized as disks of 10 mm diameter using boron nitride as a binder. Data treatment and linear combination fitting were performed with Athena software, while the details of the EXAFS fitting approach, using the GNXAS code, can be found elsewhere [68,69].

The textural properties of the samples were studied by $N_2$ adsorption performed at -196 °C on a 3Flex manometric sorption analyzer (Micromeritics, Atlanta, GA). Prior to the adsorption experiments, all samples were outgassed under vacuum for 12 h at 110 ºC. The surface area

($S_{NLDFT}$) and the pore size distribution of each material were calculated using the 2D non-local density functional theory (2D-NLDFT) with SAIEUS software (Micromeritics, Atlante, GA). The other textural characteristics were obtained from the pore size distribution profiles, such as: total pore volume, $V_T$; ultramicropore volume (pore diameter less than 0.7 nm), $V_{umicro}$; and micropore volume (pore diameter less than 2.0 nm), $V_{micro}$.

*Electrochemical characterization:* Electrochemical experiments were performed with a rotating ring-disk electrode (RRDE) in a traditional three-electrode cell using an Autolab PGSTAT302 potentiostat. The rotating electrode is equipped with a carbon disk of 5 mm of diameter and a platinum ring that works as a second working electrode. A reversible hydrogen electrode (RHE) immersed in the working electrolyte and a graphite rod were used as reference and counter electrodes, respectively.

The working electrodes were prepared as follows: 0.5 mg of TM@$CN_x$ was suspended ultrasonically in 0.125 mL of a 0.2 wt.% Nafion ® and 20 wt.% isopropanol aqueous solution [70]. 33 µL of the 4 mg $mL^{-1}$ suspension was drop-cast onto the carbon disk electrode up to a catalyst loading of 685 $\mu g \cdot cm^{-2}$.

The electrocatalytic activity towards the oxygen reduction reaction was studied by linear sweep voltammetry (LSV) in $O_2$-saturated 0.1 M KOH and 0.5 M $H_2SO_4$ solutions between 1.0 and 0.0 V vs RHE at 1600 rpm and a scan rate of 5 $mV \cdot s^{-1}$. The platinum ring potential was set at 1.5 V vs RHE to calculate the number of electrons transferred and the yield of hydrogen peroxide ($H_2O_2$) during the ORR measurements. The stability of the samples was studied by chronoamperometric tests. The working electrode was held at 0.7 V vs RHE for 10,000 s at 1600 rpm, under continuous oxygen saturation. The electrocatalytic activity towards hydrogen evolution and oxygen evolution reaction was studied by LSV in $N_2$-saturated 1.0 M KOH and 0.5 M $H_2SO_4$ solutions between 0.2 and – 1.0 V vs RHE for the HER, and 0.8 and 1.8 V vs RHE for the OER, at 1600 rpm and 5 $mV \cdot s^{-1}$.

*DFT computational details:* The electrocatalytic properties of TM-$N_4$ sites embedded in a graphene-like monolayer (G-$N_4$-TM) were revealed through periodic DFT calculations [71,72] implemented in the Vienna *ab initio* simulation package (VASP) [73,74]. The Perdew-Burke-Ernzerhof (PBE) functional within GGA approximation was used to describe the exchange–correlation interaction [75]. All the studied structures were relaxed using the conjugate gradient method. The plane wave cut-off energy was set at 700 eV, the Kohn-sham self-consistent energy [76], and the forces convergence criterion were set at $10^{-8}$ eV and 0.02 eV·Å$^{-1}$ per atom, respectively. The Brillouin zone sampling with Gamma centered mesh was set to 3 × 3 × 1 grid for geometry optimizations, and 15 × 15 × 1 for density of state (DOS) and partial density of state calculations (PDOS) (see Figures S29).

To accurately describe the adsorption of the different gas molecules, the Grimme dispersion correction (DFT-D3(BJ)) scheme [77,78] was used to effectively account for van der Waals (vdW) forces, and a Hubbard-like U parameter was included to further treat the strong correlation effects of the transition metal sites, with U values (4.0, 4.0, 3.3, 6.4, and 4.0 eV for Mn, Fe, Co, Ni, and Cu, respectively) derived from the study of Wang et al. [79].

Spin-polarized calculations were performed for all cases. Accordingly, we identified an energetically favorable square-plane nickel(II) (d8 configuration) with a low-spin diamagnetic ground state (S = 0), a cobalt(II) ($d^7$ configuration) with a low-spin ground state $(t_{2g})^6$ $(e_g)^1$ (S=1/2), and an iron(II) ($d^6$ configuration) with an intermediate spin state of S=1 (see Table S1 in Supporting Information).

To understand the interaction between the gas molecules and the G-$N_4$-TM monolayer, the adsorption energy was calculated at 0 K using the following equation:

$$\Delta E_{ads} = E_{(C-N4-M+guest)} - (E_{C-N4-M} + E_{guest}) \quad \text{Eq.1}$$

where $E_{(C-N4-M+guest)}$ is the total energy of the graphene monolayer with a single gas molecule adsorbed, and $E_{C-N4-M}$ and $E_{guest}$ are the total energies of the graphene monolayer and the isolated gas molecule, respectively.

## Supporting Information

Supporting Information is available from the Wiley Online Library or from the author.


## Acknowledgements

ANR-15-IDEX-04-LUE and, the TALiSMAN and TALiSMAN2 projects, financed by the European Regional Development Fund (ERDF), are gratefully acknowledged. JQB thanks the Ministerio de Universidades, the European Union, and the University of Alicante for the financial support (MARSALAS21-21). SGD thanks the Ministerio de Universidades, the European Union, and the University of Oviedo for the financial support (MU-21-UP2021-030 30267158).


## Conflict of Interest

The authors declare no conflict of interest.

## Data Availability Statement

The data that support the findings of this study are available from the corresponding author upon reasonable request.


Received: ((will be filled in by the editorial staff))
Revised: ((will be filled in by the editorial staff))
Published online: ((will be filled in by the editorial staff))


## References


[1] IPCC, Summary for Policymakers, in: V. Masson-Delmotte, P. Zhai, H.O. P€ortner, D.

Roberts, J. Skea, P.R. Shukla, A. Pirani, W. Moufouma-Okia, C. Péan, R. Pidcock, S. Connors, J.B.R. Matthews, Y. Chen, X. Zhou, M.I. Gomis, E. Lonnoy, T. Maycock, M. Tignor, (n.d.).

[2] United Nations Framework Convention on Climate Chenge, Paris Agreement (Annex to Decision 1/CP.21, 2015 document FCCC/CP/201510/Add.1 Paris: United Nations. Retrieved from hhtp://unfcc.int/resource/docs/2015/cop21/eng/10a01.pdf., (n.d.).

[3] J. Quílez-Bermejo, E. Morallón, D. Cazorla-Amorós, *Carbon* **2020**, *165*, 434.

[4] X. Li, L. Zhao, J. Yu, X. Liu, X. Zhang, H. Liu, W. Zhou, *Nano-Micro Lett.* **2020**, *12*, 131.

[5] M. Winter, R. J. Brodd, *Chem. Rev.* **2004**, *104*, 4245.

[6] Y. Sahai, *Fundamentals of Electrochemical Energy Devices*, **2021**.

[7] L. Li, P. Wang, Q. Shao, X. Huang, *Adv. Mater.* **2021**, *33*, 2004243.

[8] J. Zhu, L. Hu, P. Zhao, L. Y. S. Lee, K.-Y. Wong, *Chem. Rev.* **2020**, *120*, 851.

[9] A. Morozan, B. Jousselme, S. Palacín, *Energy Environ. Sci.* **2011**, *4*, 1238.

[10] J. Wang, J. Kim, S. Choi, H. Wang, J. Lim, *Small Methods* **2020**, *4*, 2000621.

[11] Y. Wang, D. Wang, Y. Li, *Adv. Mater.* **2021**, *33*, 2008151.

[12] J. Cai, R. Javed, D. Ye, H. Zhao, J. Zhang, *J. Mater. Chem. A* **2020**, *8*, 22467.

[13] T. Sun, S. Mitchel, J. Li, P. Lyu, X. Wu, J. Pérez-Ramírez, J. Lu, *Adv. Mater.* **2021**, *33*, 2003075.

[14] C. Zhu, S. Fu, Q. Shi, D. Du, Y. Lin, *Angew. Chemie - Int. Ed.* **2017**, *56*, 13944.

[15] B. W. Zhang, Y. X. Wang, S. L. Chou, H. K. Liu, S. X. Dou, *Small Methods* **2019**, *3*,

1800497.

[16] T. Sharifi, E. Gracia-Espino, A. Chen, G. Hu, T. Wagberg, *Adv. Energy Mater.* **2020**, *10*, 1902084.

[17] J. Kossmann, T. Heil, M. Antonietti, N. López-Salas, *ChemSusChem* **2020**, *13*, 6643.

[18] J. Kossmann, D. Piankova, N. V. Tarakina, J. Heske, T. D. Kühne, J. Schmidt, M. Antonietti, N. López-Salas, *Carbon* **2021**, *172*, 497.

[19] N. López-Salas, J. Kossmann, M. Antonietti, *Acc. Mater. Res.* **2020**, *1*, 117.

[20] H. Wang, W. Wang, Y. Y. Xu, S. Dong, J. Xiao, F. Wang, H. Liu, B. Y. Xia, *ACS Appl. Mater. Interfaces* **2017**, *9*, 10610.

[21] Y. Wang, Q. Li, L.-C. Zhang, Y. Wu, H. Chen, T. Li, M. Xu, S.-J. Bao, *J. Mater. Chem. A* **2021**, *9*, 7137.

[22] K. Hu, L. Tao, D. Liu, J. Huo, S. Wang, *ACS Appl. Mater. Interfaces* **2016**, *8*, 19379.

[23] J. Quílez-Bermejo, M. Melle-Franco, E. San-Fabián, E. Morallón, D. Cazorla-Amorós, *J. Mater. Chem. A* **2019**, *7*, 24239.

[24] J. Li, P. Prslja, T. Shinagawa, A. J. . Fernández, F. Krumeich, K. Artyushkova, P. Atanassov, A. Zitolo, Y. Zhou, R. García-Muelas, N. Lopez, J. Pérez-Ramírez, F. Jaouen, *ACS Catal.* **2019**, *9*, 10426.

[25] D. Karapinar, N. T. Huan, N. R. Sahraie, J. Li, D. Wakerley, N. Touati, S. Zanna, D. Taverna, L. H. G. Tizei, A. Zitolo, F. Jaouen, V. Mougel, M. Fontecave, *Angew. Chemie - Int. Ed.* **2019**, *58*, 15098.

[26] H. Dierkes, R. Dronskowski, *J. Inorg. Gen. Chem.* **2014**, *640*, 3148.

[27] X. Wan, W. Chen, J. Yang, M. Liu, X. Liu, J. Shui, *ChemElectroChem* **2019**, *6*, 304.

[28] A. Dessalle, J. Quílez-Bermejo, V. Fierro, F. Xu, A. Celzard, *Carbon* **2023**, *203*, 237.

[29] Y. Wang, L. Wang, Y. Xie, M. Tong, C. Tian, H. Fu, *ACS Sustain. Chem. Eng.* **2022**, *10*, 3346.

[30] Y. Qin, Z. Ou, C. Xu, Q. Lan, R. Jin, X. Xu, C. Guo, H. Li, Y. Si, *Chem. Eng. J.* **2022**, *440*, 135650.

[31] J. Quílez-Bermejo, E. Morallón, Cazorla-Amorós, *Chem. Commun.* **2018**, *54*, 4441.

[32] J. Quílez-Bermejo, S. Pérez-Rodríguez, R. L. S. Canevesi, D. Torres, E. Morallón, D. Cazorla-Amorós, A. Celzard, V. Fierro, *Carbon* **2022**, *196*, 708.

[33] J. Li, M. T. Sougrati, A. Zitolo, J. M. Ablett, I. C. Oguz, T. Mineva, I. Matanovic, P. Atanassov, Y. Huang, I. Zenyuk, A. Di Cicco, K. Kumar, L. Dubau, F. Maillard, G. Drazic, F. Jaouen, *Nat. Catal.* **2021**, *4*, 10.

[34] Y. Yang, K. Mao, S. Gao, H. Huang, G. Xia, Z. Lin, P. Jian, C. Wang, H. Wang, Q. Chen, *Adv. Mater.* **2018**, *30*, 1801732.

[35] H. Shang, W. Sun, R. Sui, J. Pei, L. Zheng, J. Dong, Z. Jiang, D. Zhou, Z. Zhuang, W. Chen, J. Zhang, D. Wang, Y. Li, *Nano Lett.* **2020**, *20*, 5443.

[36] Z.-Y. Wu, X.-X. Xu, B.-C. Hu, H.-W. Liang, Y. Lin, L.-F. Chen, S.-H. Yu, *Angew. Chemie - Int. Ed.* **2015**, *54*, 8179.

[37] Q. Li, W. Chen, H. Xiao, Y. Gong, Z. Li, L. Zheng, Z. Zheng, W. Yang, W.-C. Cheong, R. Shen, N. Fu, L. Gu, Z. Zhuang, C. Chen, D. Wang, Q. Peng, J. Li, Y. Li, *Adv. Mater.* **2018**, *30*, 1800588.

[38] Y. Guo, F. Liu, L. Feng, X. Wang, X. Zhang, J. Liang, *Chem. Eng. J.* **2022**, *429*, 132150.

[39] Y. Wang, L. Chen, Z. Mao, L. Peng, R. Xiang, X. Tang, J. Deng, Z. Wei, Q. Liao, *Sci. Bull.* **2019**, *64*, 1095.

[40] C. Shi, Y. Liu, R. Qi, J. Li, J. Zhu, R. Yu, S. Li, X. Hong, J. Wu, S. Xi, L. Zhou, L. Mai, *Nano Energy* **2021**, *87*, 106153.

[41] X. Song, N. Li, H. Zhang, L. Wang, Y. Yan, H. Wang, L. Wang, Z. Bian, *ACS Appl. Mater. Interfaces* **2020**, *12*, 17519.

[42] J. Chen, H. Li, C. Fan, Q. Meng, Y. Tang, X. Qiu, G. Fu, T. Ma, *Adv. Mater.* **2020**, *32*, 2003134.

[43] W. Wu, Y. Liu, D. Liu, W. Chen, Z. Song, X. Wang, Y. Zheng, N. Lu, C. Wang, J. Mao, Y. Li, *Nano Res.* **2021**, *14*, 998.

[44] L. Bai, C. Hou, X. Wen, J. Guan, *ACS Appl. Energy Mater.* **2019**, *2*, 4755.

[45] J. Quílez-Bermejo, K. Strutynski, M. Melle-Franco, E. Morallón, D. Cazorla-Amorós, *ACS Appl. Mater. Interfaces* **2020**, *12*, 54815.

[46] Z. W. She, J. Kibsgaard, C. F. Dickens, I. Chorkendorff, J. K. Norskov, T. F. Jaramillo, *Science* **2017**, *355*, 6321.

[47] J. K. Norskov, J. Rossmeisl, A. Logadottir, L. Lindqvist, J. R. Kitchin, T. Bligaard, H. Jonsson, *J. Phys. Chem. B* **2004**, *108*, 17886.

[48] X. Chen, R. Hu, *Int. J. Hydrogen Energy* **2019**, *44*, 15409.

[49] Y. J. Sa, S. O. Park, G. Y. Jung, T. J. Shin, H. Y. Jeong, S. K. Kwak, S. H. Joo, *ACS Catal.* **2019**, *9*, 83.

[50] J. Yu, J. Li, C. Y. Xu, J. Liu, R. Chen, J. Zhu, R. Li, J. Wang, *Carbon* **2021**, *185*, 96.

[51] L. Cao, Q. Luo, W. Liu, Y. Lin, X. Liu, Y. Cao, W. Zhang, Y. Wu, J. Yang, T. Yao, S.

Wei, *Nat. Catal.* **2019**, *2*, 134.

[52] C. Lei, Y. Wang, Y. Hou, P. Liu, J. Yang, T. Zhang, X. Zhuang, M. Chen, B. Yang, L. Lei, C. Yuan, M. Qiu, X. Feng, *Energy Environ. Sci.* **2019**, *12*, 149.

[53] S. Li, Q. Zhou, G. Yu, Z. Lei, Z. Liu, Q. Xu, W. Xu, R. Wu, *Appl. Surf. Sci.* **2020**, *518*, 146239.

[54] J. Jiang, L. Zhu, Y. Sun, Y. Chen, H. Chen, S. Han, H. Lin, *J. Power Sources* **2019**, *426*, 74.

[55] S. Chao, Q. Xia, G. Wang, X. Zhang, *Int. J. Hydrogen Energy* **2019**, *44*, 4707.

[56] J. Li, Y. Wang, T. Shou, H. Zhang, X. Sun, J. Tang, L. Zhang, A. M. Al-Enizi, Z. Yang, G. Zheng, *J. Am. Chem. Soc.* **2015**, *137*, 14305.

[57] M. A. Ahsan, A. R. P. Santiago, Y. Hong, N. Zhang, M. Cano, E. Rodriguez-Castellón, L. Echegoyen, S. T. Sreenivasan, J. C. Noveron, *J. Am. Chem. Soc.* **2020**, *142*, 14688.

[58] S. Cui, M. Qian, X. Liu, Z. Sun, P. Du, *ChemSusChem* **2016**, *9*, 2365.

[59] H. Zhang, Y. Liu, T. Chen, J. Zhang, J. Zhang, X. W. Lou, *Adv. Mater.* **2019**, *31*, 1904585.

[60] Y. Zheng, G. Zhang, P. Zhang, S. Chu, D. Wu, C. Sun, B. Qian, S. Chen, S. Tao, L. Song, *Chem. Eng. J.* **2022**, *429*, 132122.

[61] J. Xu, L. Shi, C. Liang, H. Wu, J. Lei, D. Liu, D. Qu, Z. Xie, J. Li, H. Tang, *ChemElectroChem* **2017**, *4*, 1148.

[62] Y. Pan, S. Liu, K. Sun, X. Chen, B. Wang, K. Wu, X. Cao, W. C. Cheong, R. Shen, A. Han, Z. Chen, L. Zheng, J. Luo, Y. Lin, Y. Liu, D. Wang, Q. Peng, Q. Zhang, C. Chen, Y. Li, *Angew. Chemie - Int. Ed.* **2018**, *57*, 8641.

[63] S. Dilpazir, H. He, Z. Li, M. Wang, P. Lu, R. Liu, Z. Xie, D. Gao, G. Zhang, *ACS Appl. Energy Mater.* **2018**, *1*, 3283.

[64] Y. Gao, H. Zhao, D. Chen, C. Chen, F. Ciucci, *Carbon* **2015**, *94*, 1028.

[65] L. Yang, L. Shi, D. Wang, Y. Lv, D. Cao, *Nano Energy* **2018**, *50*, 691.

[66] Y. Li, Z.-S. Wu, P. Lu, X. Wang, W. Liu, Z. Liu, J. Ma, W. Ren, Z. Jiang, X. Bao, *Adv. Sci.* **2020**, *7*, 1903089.

[67] W. Zha, D. Liu, Z. Ma, Y. Wang, Y. Wei, X. Ma, L. Wang, Q. Zhang, B. Lou, R. Yuan, X. Fu, R. Sa, *Appl. Surf. Sci.* **2021**, *564*, 150331.

[68] A. Filipponi, A. Di Cicco, C. R. Natoli, *Phys. Rev. B Condens. Matter.* **1995**, *52*, 15135.

[69] A. Filipponi, A. Di Cicco, C. R. Natoli, *Phys. Rev. B Condens. Matter.* **1995**, *52*, 15122.

[70] L. Bouleau, S. Pérez-Rodríguez, J. Quílez-Bermejo, M. T. Izquierdo, F. Xu, V. Fierro, A. Celzard, *Carbon* **2022**, *189*, 349.

[71] L. J. Sham, W. Kohn, *Phys. Rev.* **1966**, *145*, 561.

[72] P. Hohenberg, W. Kohn, *Phys. Rev.* **1964**, *136*, B864.

[73] G. Kresse, J. Hafner, *Phys. Rev. B* **1993**, *47*, 558.

[74] G. Kresse, J. Furthmüller, *Comput. Mater. Sci.* **1996**, *6*, 15.

[75] J. P. Perdew, K. Burke, M. Ernzerhof, *Phys. Rev. Lett.* **1996**, *77*, 3865.

[76] W. Kohn, L. J. Sham, *Phys. Rev.* **1965**, *140*, A1133.

[77] S. Grimme, S. Ehrlich, L. Goerigk, *J. Comput. Chem.* **2011**, *32*, 1456.

[78] S. Grimme, J. Antony, S. Ehrlich, H. Krieg, *J. Chem. Phys.* **2010**, *132*, 154104.

[79] L. Wang, T. Maxisch, G. Ceder, *Phys. Rev. B* **2006**, *73*, 195107.

Javier Quílez-Bermejo[1,2,*], Sergio García-Dalí[1,3], Andrea Zitolo[4], Rafael Canevesi[1], María T. Izquierdo[5], Alain Celzard[1], Vanessa Fierro[1;*]

# Advanced Design of Metal Nanoclusters and Single Atoms Embedded in $C_1N_1$-derived Carbon Materials for ORR, HER and OER

# Supporting Information

## Advanced Design of Metal Nanoclusters and Single Atoms Embedded in $C_1N_1$-derived Carbon Materials for ORR, HER and OER

*Javier Quílez-Bermejo*[1,2,*], *Sergio García-Dalí*[1,3], *Ayoub Daouli*[4], *Andrea Zitolo*[5], *Rafael Canevesi*[1], *Mélanie Emo*[6], *María T. Izquierdo*[7], *Michael Badawi*[4], *Alain Celzard*[1,8], *Vanessa Fierro*[1,*]

[1]Université de Lorraine, Centre National de la Recherche Scientifique (CNRS), Institut Jean Lamour (IJL), F-88000, Épinal, France.

[2]Departamento de Química Inorgánica and Instituto de Materiales, Universidad de Alicante, Ap. 99, 03080, Spain.

[3]Departamento de Ciencia de los Materiales e Ingenieria Metalúrgica, Universidad de Oviedo, 33004, Oviedo, Spain.

[4]Laboratoire de Physique et Chimie Théoriques (LPCT), UMR 7019 CNRS, Université de Lorraine, F-54000 Nancy, France

[5]Synchrotron SOLEIL, L'orme des Merisiers, BP 48 Saint Aubin, Gif-sur-Yvette, France.

[6]Université de Lorraine, Centre national de la Recherche Scientifique (CNRS), Institut Jean Lamour (IJL), 54011 Nancy, France

[7]Instituto de Carboquímica (ICB-CSIC), Miguel Luesma Castán 4, E-50018, Zaragoza, Spain.

[8]Institut Universitaire de France (IUF), France.

## 1. Stability of the G−$N_4$−TM structures

Table S6 summarizes the equilibrium bond distances and magnetic properties of the three selected G-$N_4$-Fe, G-$N_4$-Co, and G-$N_4$-Ni systems at different spin states. It is well known that, depending on their coordination number, some transition metals exist in different spin states (i.e., high or low spin states). In the present scenario, the stability of the TM-$N_4$ center can be understood through the charge rearrangement between the nitrogen dangling bonds that take the two 4s electrons of the metal, thus forming the $TM(^{2+}) - N_4(^{2-})$ complex. Accordingly, we identified an energetically favorable square-plane nickel(II) ($d^8$ configuration) with a low-spin diamagnetic ground state (S = 0), a cobalt(II) ($d^7$ configuration) with a low-spin ground state $(t_{2g})^6$ $(e_g)^1$ (S=1/2), and an iron(II) ($d^6$ configuration) with an intermediate spin state of S=1. Consequently, this indicates that the spin polarization of the π electrons in the vicinity of our preselected metal atom is weak.

## 2. $O_2$ Interaction with the Fe–$N_4$ Center

The adsorption of $O_2$ on the Fe center is the most important intermediate when investigating its ORR activity. Previous investigations reported two equilibrium orientations of the $O_2$ molecule when chemisorbed on a transition metal: (i) one oxygen atom bound to the metal center, denoted here as end-on (see Table S7, inset a), and (ii) two oxygen atoms bound to the metal center, denoted as side-on (see Table S7, inset b). Due to the unpaired electrons of the Fe (II) metal site and the $O_2$ molecule, the appearance of the stable Fe-$O_2$ end product is ensured by their spin coupling. Therefore, to identify a stable adsorption configuration, a systematic calculation was performed considering the end-on and side-on geometries, along with the different spin states of iron (II).

Table S7 lists our results for the adsorption of $O_2$ on the metal center of G-$N_4$-Fe. Our results revealed exothermic adsorption in both $O_2$ geometries (side-on and end-on) and in three Fe(II)

spin states (singlet, triplet and quintet). We find that the first ground state is end-on-triplet with an $O_2$ binding energy of -1.63 eV, while the first excited state is side-on-quintet 0.03 eV slightly higher in energy, as can be seen in Table S7. The metallic iron atom tends to move out of the material plane along with the magnetic moment change. The out-of-plane dislocation can reach a length of 0.74 Å with an intermediate spin state when $O_2$ is laterally adsorbed.

## 3. Calculation methods of evaluating ORR, OER and HER activity

The aim here is to reveal the mechanism of oxygen evolution reaction (OER), oxygen reduction reaction (ORR), and hydrogen evolution reaction (HER) for the best promising materials. It has been proposed that under acidic conditions, at the pressure of 1 bar and temperature of 298.15 K, the reaction on G-$N_4$-TM takes place through four proton-coupled electron transfer (PCET) steps:

**Oxygen Evolution Reaction (OER) for G-$N_4$-Ni**

$$* + H_2O \rightarrow OH^* + H^+ + e^-, \quad \text{(Eq.S1)}$$

$$OH^* \rightarrow O^* + H^+ + e^-, \quad \text{(Eq.S2)}$$

$$O^* + H_2O \rightarrow OOH^* + H^+ + e^-, \quad \text{(Eq.S3)}$$

$$OOH^* \rightarrow * + O_2(g) + H^+ + e^-, \quad \text{(Eq.S4)}$$

**Oxygen Reduction Reaction (ORR) for G-$N_4$-Fe**

$$* + O_2 + (H^+ + e^-) \rightarrow OOH^*, \quad \text{(Eq.S5)}$$

$$OOH^* + (H^+ + e^-) \rightarrow O^* + H_2O, \quad \text{(Eq.S6)}$$

$$O^* + (H^+ + e^-) \rightarrow OH^*, \quad \text{(Eq.S7)}$$

$$OH^* + (H^+ + e^-) \rightarrow * + H_2O, \quad \text{(Eq.S8)}$$

where the asterisk (*) represents the subsequent intermediate species adsorbed onto the active site of the G-$N_4$-Fe and G-$N_4$-Ni catalysts for ORR and OER, respectively.

The computational hydrogen electrode (CHE) method, developed by Nørskov et al., allows approximating the free energy differences corresponding to these four PCET steps. Hence the free energies of the OER reaction (i.e., (1), (2), (3), and (4)):

$$\Delta G_1 = G(HO^*) + G(H^+) + \mu(e^-) - G(*) - G(H_2O) \quad \text{(Eq.S9)}$$

$$\Delta G_2 = G(O^*) + 2\,G(H^+) + 2\,\mu(e^-) - G(*) - G(H_2O) \quad \text{(Eq.S10)}$$

$$\Delta G_3 = G(HOO^*) + 3\,G(H^+) + 3\,\mu(e^-) - G(*) - 2G(H_2O) \quad \text{(Eq.S11)}$$

$$\Delta G_4 = G(O_2) + 4\,G(H^+) + 4\,\mu(e^-) - 2\,G(H_2O) \quad \text{(Eq.S12)}$$

Similarly, for the ORR reaction (i.e., (5), (6), (7), and (8)) the free energies are given by:

$$\Delta G_5 = G(OOH^*) - G(H^+) - \mu(e^-) - G(O_2) - G(*) \quad \text{(Eq.S13)}$$

$$\Delta G_6 = G(O^*) + G(H_2O) - 2\,G(H^+) - 2\,\mu(e^-) - G(O_2) - G(*) \quad \text{(Eq.S14)}$$

$\Delta G_7 = G(OH^*) - 3\,G(H^+) - 3\,\mu(e^-) - G(O_2) - G(^*) + G(H_2O)$ (Eq.S15)

$\Delta G_8 = 2\,G(H_2O) - 4G(H^+) - 4\,\mu(e^-) - G(O_2)$ (Eq.S16)

where G (Gibbs free energy) and $\mu$ (chemical potential) are represented by:

$G = E_{DFT} + ZPE - TS$ (Eq.S17)

$G(H^+) - \mu(e^-) = \frac{1}{2}\,G(H_2)$ (Eq.S18)

where ZPE is the zero-point energy, T represents the temperature and S is the entropy.

**Reaction Gibbs free energy of hydrogen adsorption on the G-$N_4$-Co**

The HER catalytic activity of G-$N_4$-Co can be evaluated by the change of the reaction Gibbs free energy of hydrogen adsorption ($\Delta G_H^*$) given by:

$\Delta G_H^* = \Delta E_H + \Delta E_{ZPE} - T\Delta S_H$ (Eq.S19)

where $\Delta E_H$, $\Delta E_{ZPE}$ and $\Delta S_H$ are the differences of hydrogen adsorption energy, zero-point energy and entropy between adsorbed hydrogen and hydrogen in the gas phase, respectively.

## 4. Density of states calculations

Since electrical conductivity is required to facilitate the charge transport necessary for ORR, HER, and OER activities, the electronic structure of TM@CNx materials was computed from the G-$N_4$-TM configurations. Correspondingly, all five studied G-$N_4$-TM centers exhibit electronically conductive properties. Figure S29 displays the spin-resolved density of states (DOS) of the investigated TM-$N_4$ centers near the Fermi level energy. We observe that the G-$N_4$-Cu (Figure 29b) material reveals a metallic property, while all other systems present a

semiconducting character with a small band gap. Furthermore, the DOS calculations were consistent with the magnetization calculations detailed in Table S6, showing a slight magnetism for the case of G-$N_4$-Co (Figure S29a), G-$N_4$-Fe (Figure S29c), and G-$N_4$-Mn (Figure S29d), while a diamagnetic behavior was observed for G-$N_4$-Cu (Figure S29b) and G-$N_4$-Ni (Figure S29e).

The PDOS shown correspond to the 3d orbital of the metal atom, and the 2p orbital of the nitrogen and carbon atoms. As discussed above, the TM-$N_4$ center is stabilized by the charge rearrangement between the nitrogen dangling bonds that take the two 4s electrons of the metal. Therefore, the metal 3d orbitals in Figure S29 show no significant hybridization with the carbon atoms.

## Supplementary Figures and Tables

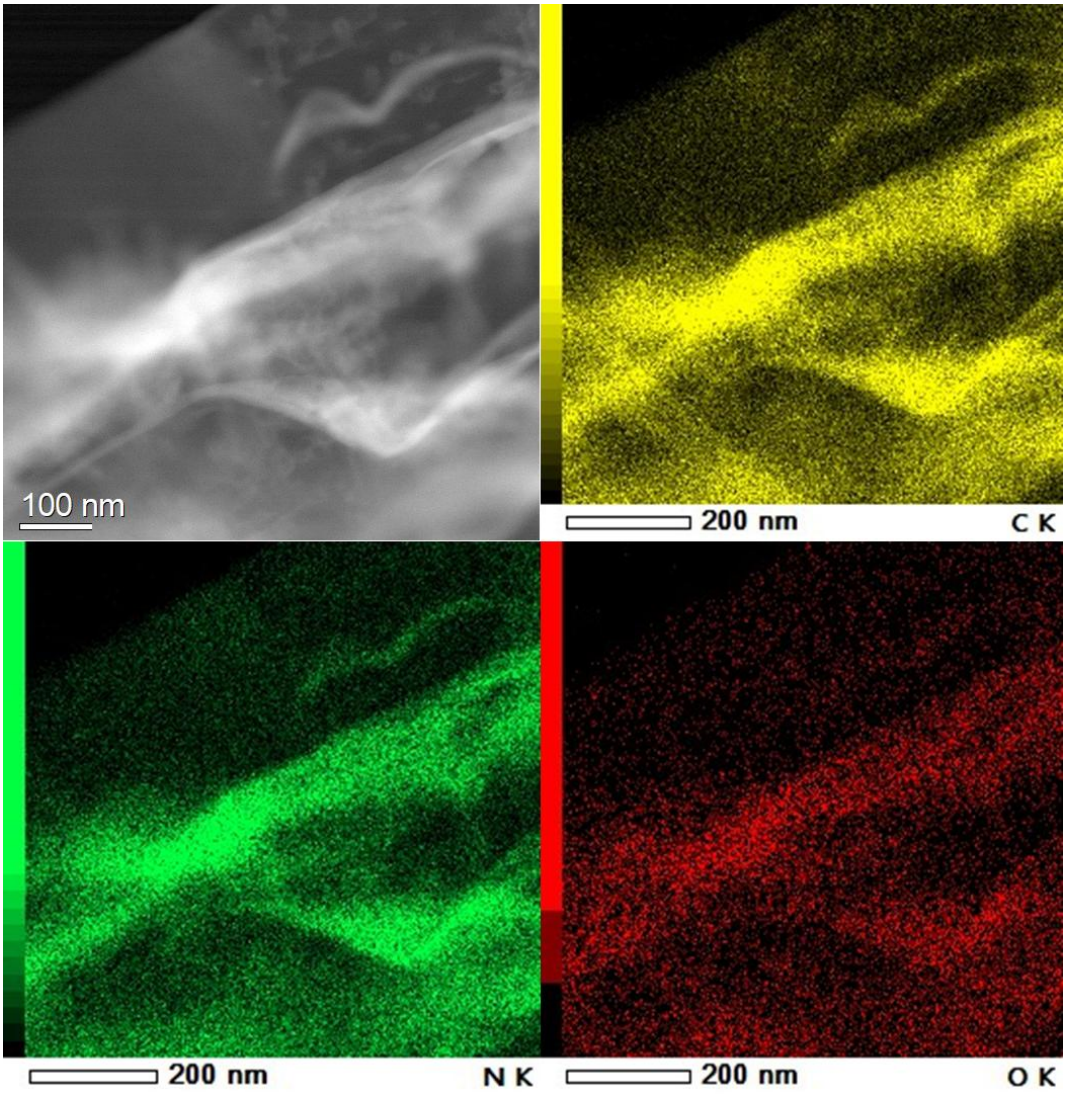


Figure S1: TEM images at low magnification (top left), and corresponding EDX mapping of carbon (yellow), nitrogen (green) and oxygen (red) of the $C_1N_1$ material.

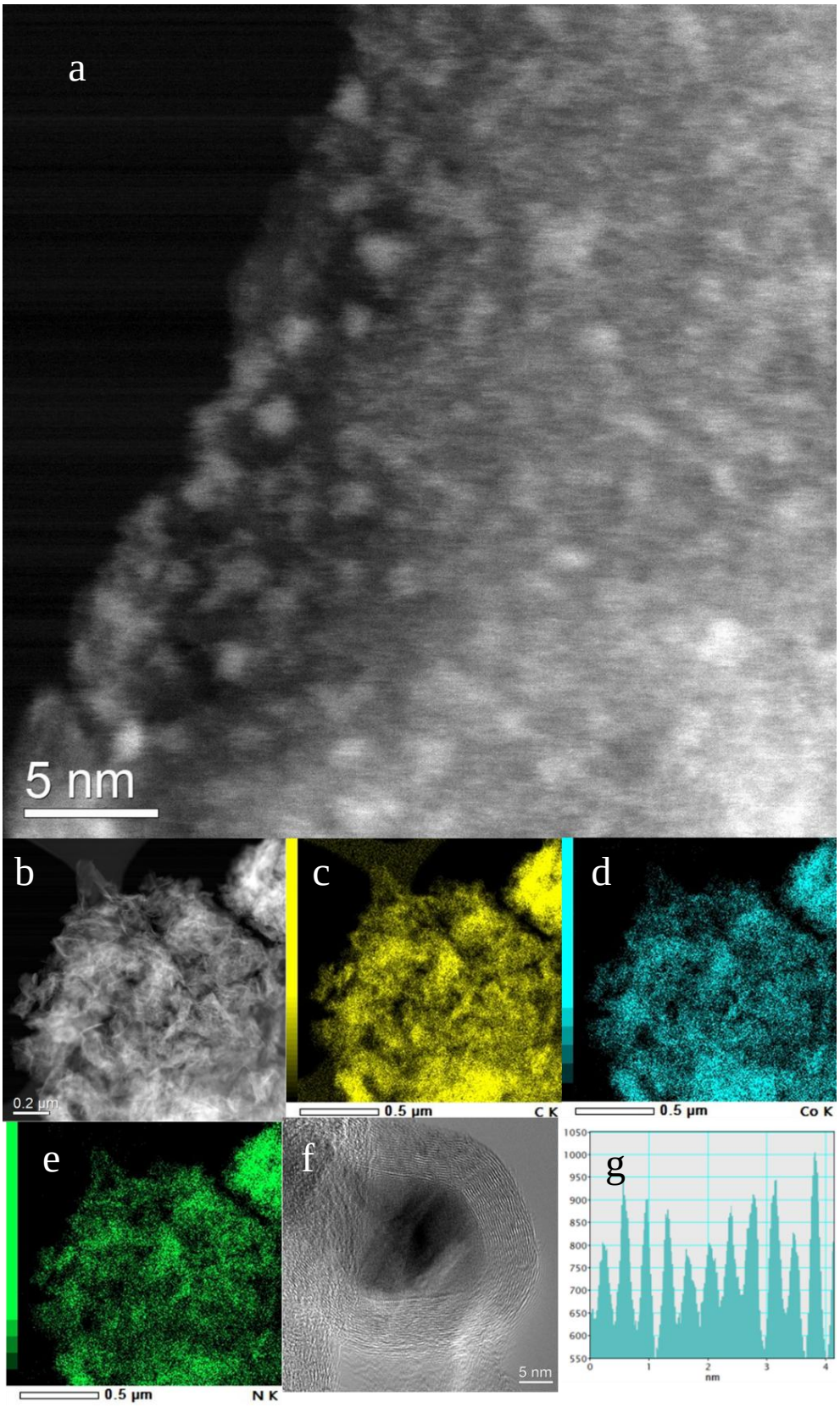


Figure S2: (a) High-magnification HAADF-STEM image of $Co@CN_x$. (b) TEM image at low magnification of $Co@CN_x$. (c-e) EDX mapping of carbon, cobalt and nitrogen. (f) High-resolution TEM image of a core-shell nanocluster in $Co@CN_x$. (g) EELS line-scan profile of the graphene-type lamellar arrangement.

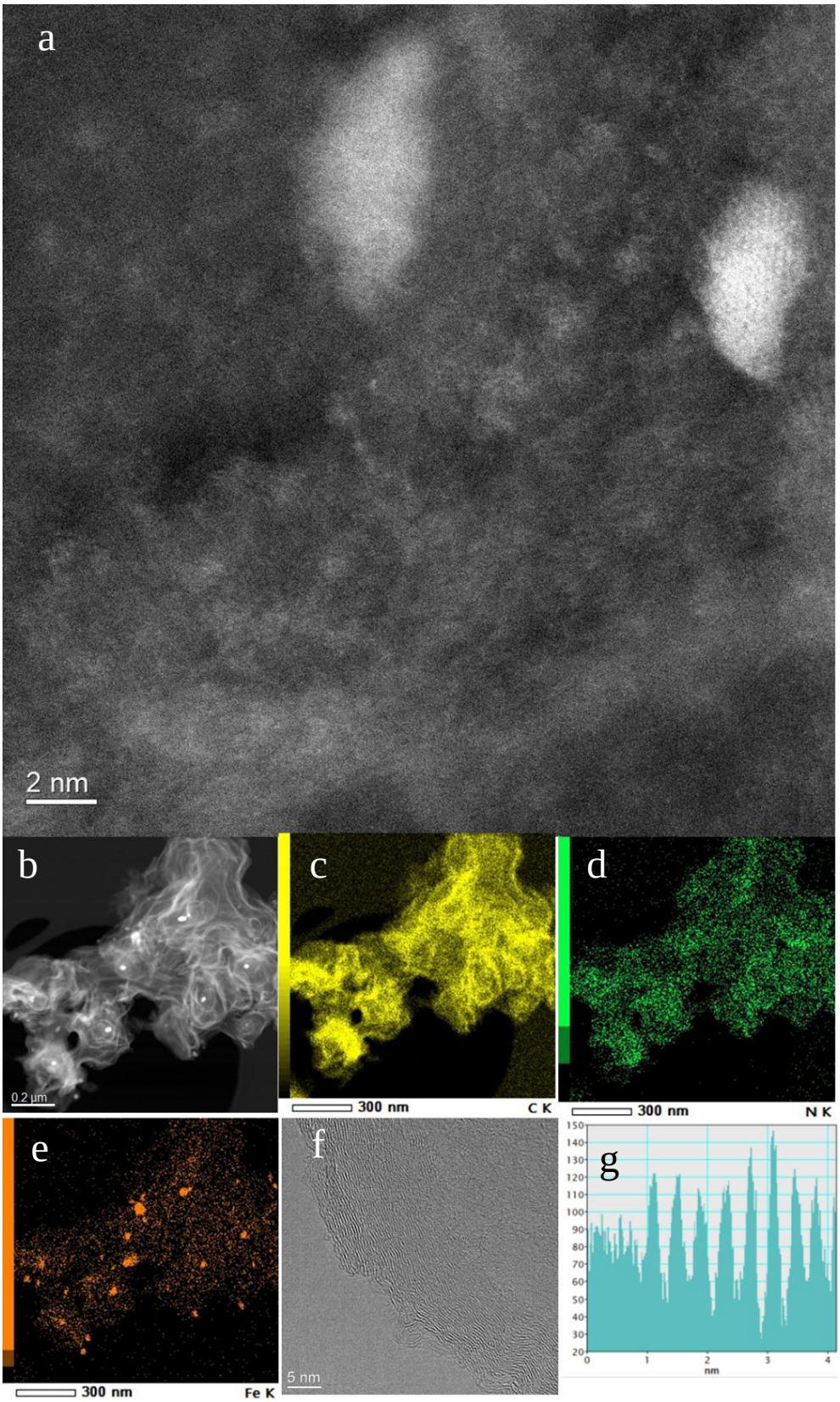


Figure S3: (a) High-magnification HAADF-STEM image of Fe@$CN_x$. (b) TEM image at low magnification of Fe@$CN_x$. (c-e) EDX mapping of carbon, nitrogen and iron. (f) High-resolution TEM image of the lamellar arrangement of carbon layers in Fe@$CN_x$. (g) EELS line-scan profile of the graphene-type lamellar arrangement.

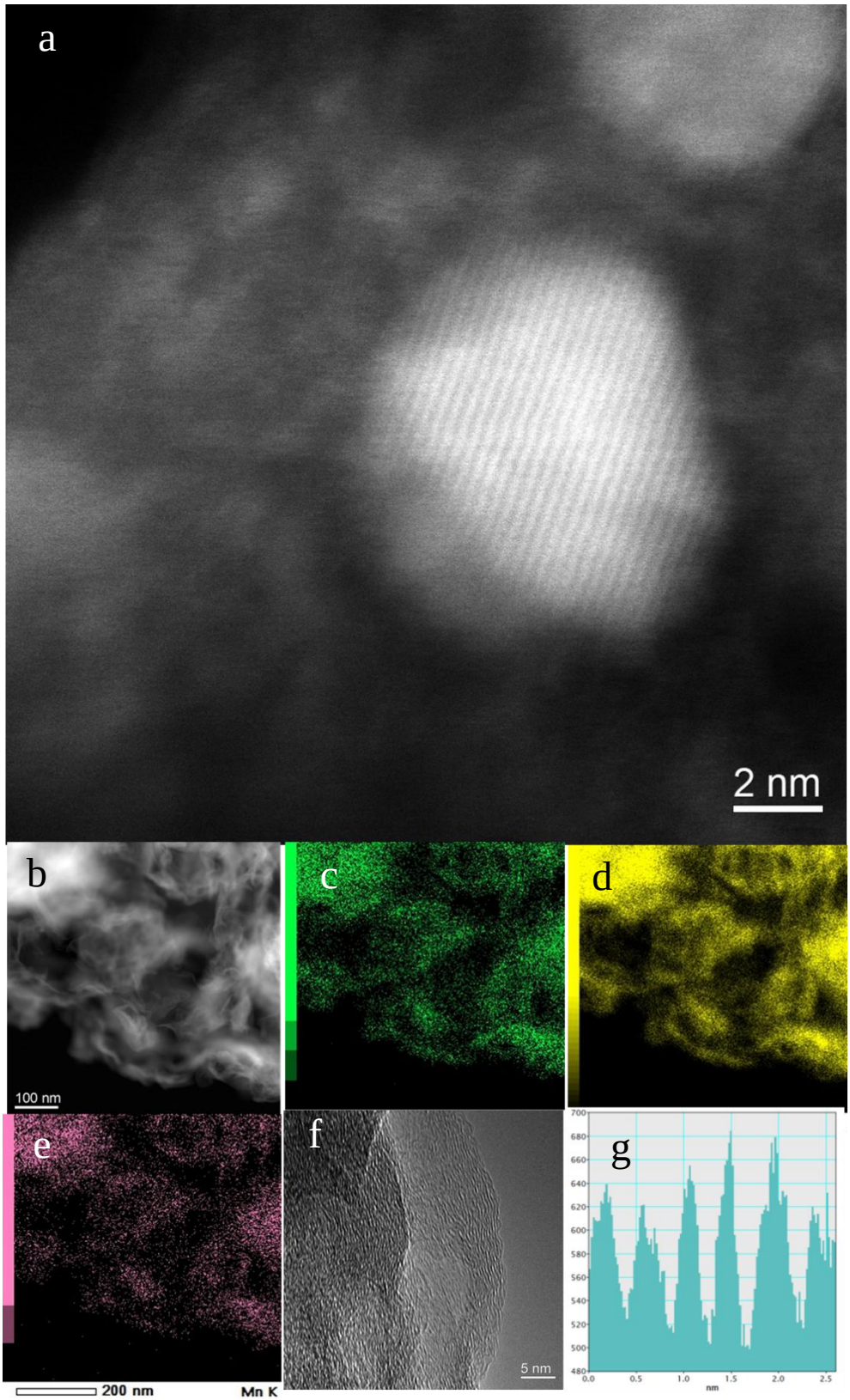


Figure S4: (a) High-magnification HAADF-STEM image of $Mn@CN_x$. (b) TEM image at low magnification of $Mn@CN_x$. (c-e) EDX mapping of carbon, nitrogen and manganese. (f) High-resolution TEM image of the lamellar arrangement of carbon layers in $Mn@CN_x$. (g) EELS line-scan profile of the graphene-type lamellar arrangement.

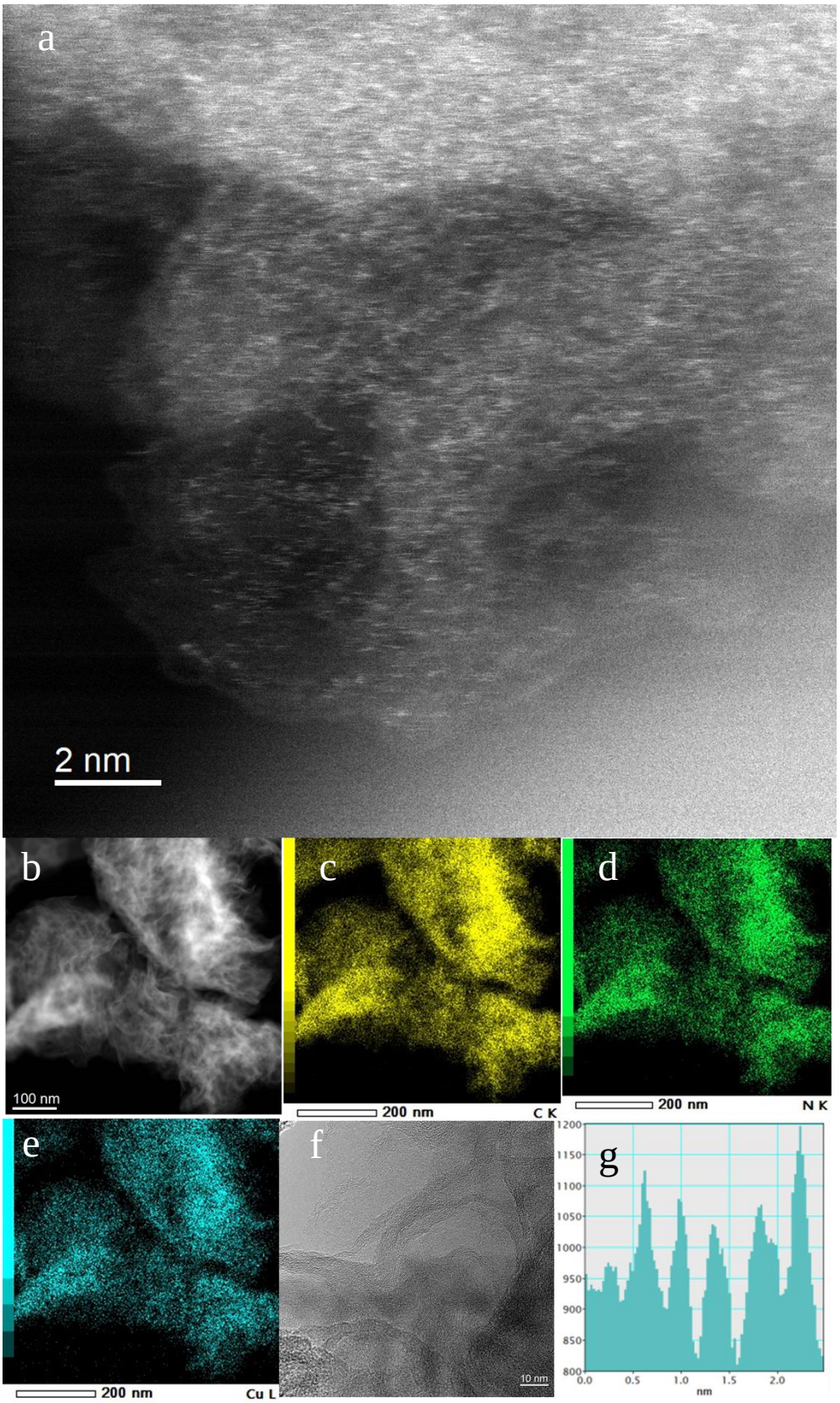


Figure S5: (a) High-magnification HAADF-STEM image of $Cu@CN_x$. (b) TEM image at low magnification of $Cu@CN_x$. (c-e) EDX mapping of carbon, nitrogen and copper. (f) High-resolution TEM image of the lamellar arrangement of carbon layers in $Cu@CN_x$. (g) EELS line-scan profile of the graphene-type lamellar arrangement.

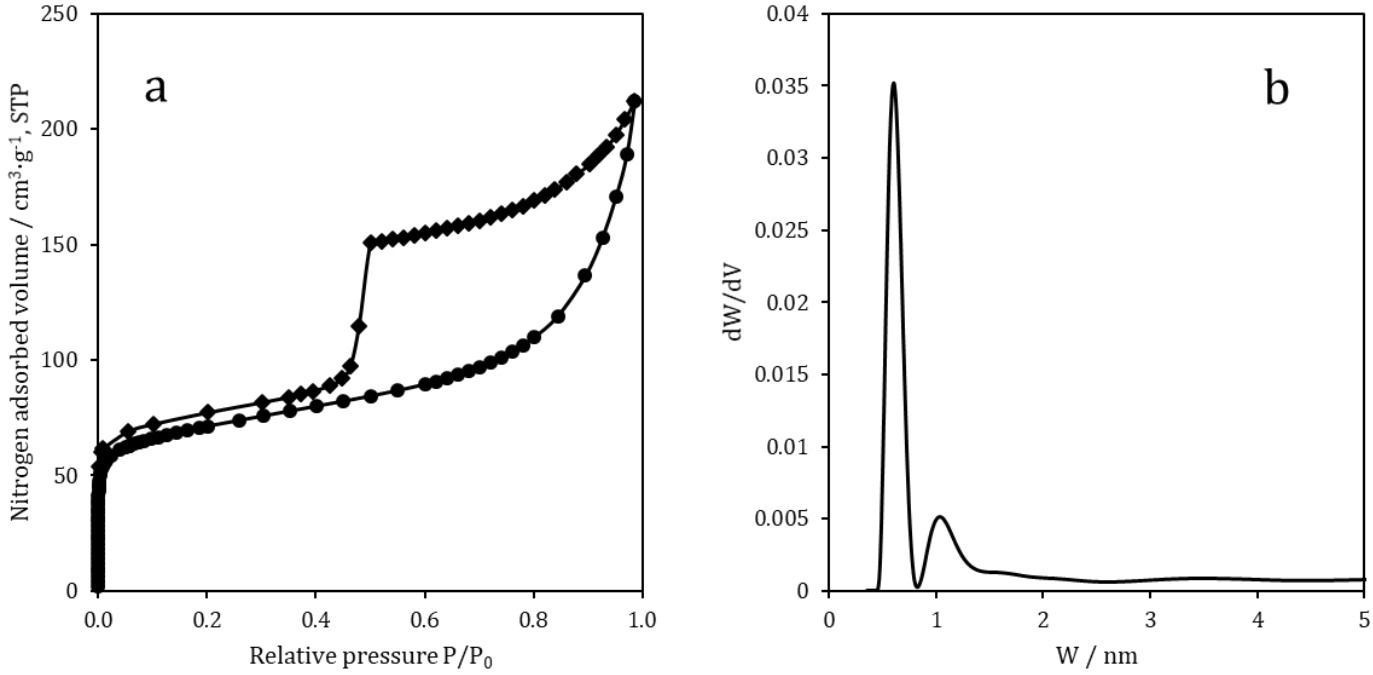


Figure S6: (a) $N_2$ adsorption-desorption isotherms, and (b) pore size distribution of the pristine $C_1N_1$ material. W represents the pore width and V represents the volume of adsorbed nitrogen. In the pore size distribution, a clear contribution at about 0.5-0.8 nm is observed, which confirms the presence of internal cavities in the $C_1N_1$ material.

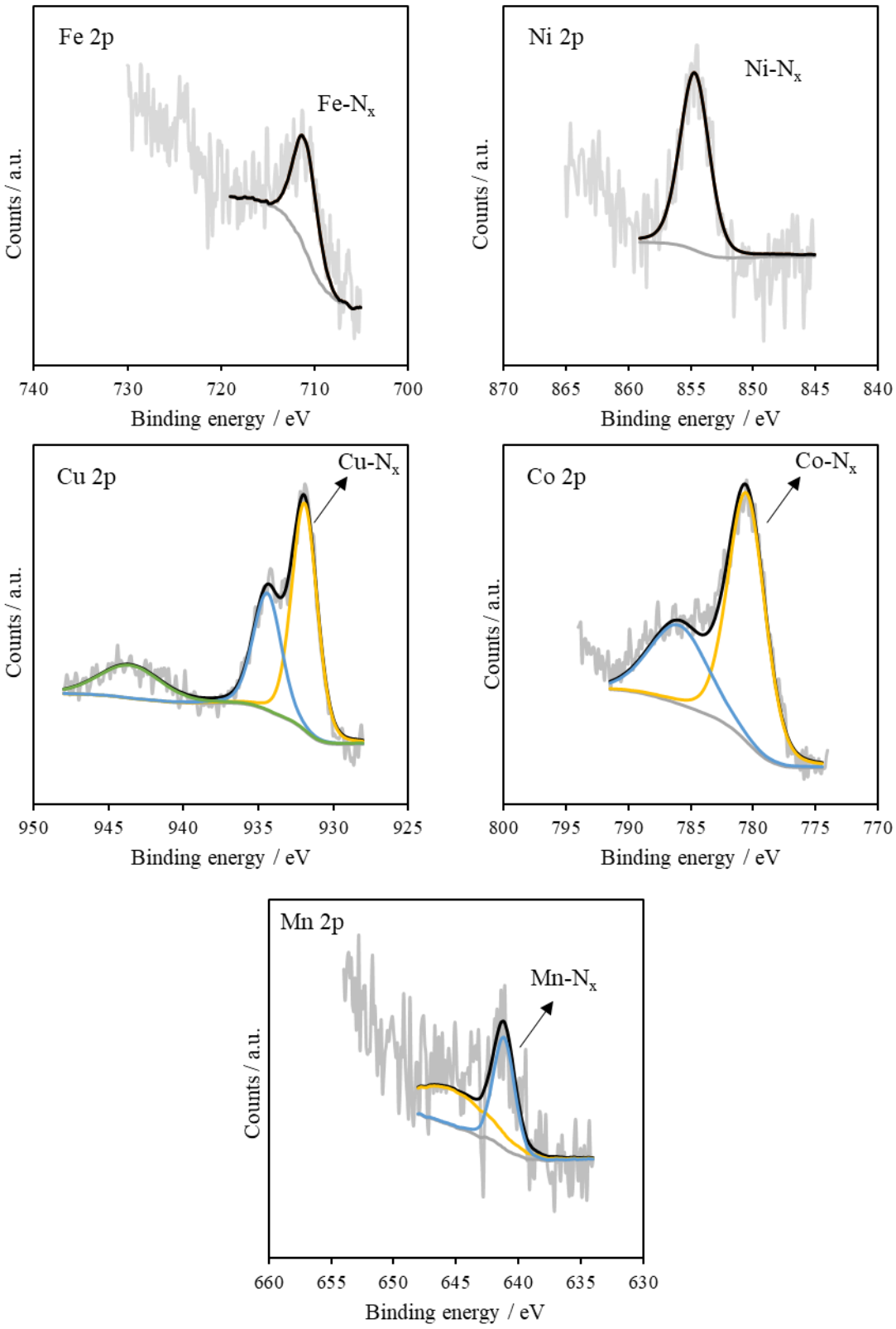


Figure S7: Fe2p, Ni2p, Cu2p, Co2p and Mn2p specta of Fe@$CN_x$, Ni@$CN_x$, Cu@$CN_x$, Co@$CN_x$ and Mn@$CN_x$, respectively. In all materials, the peak related to metal-N species was detected and highlighted.

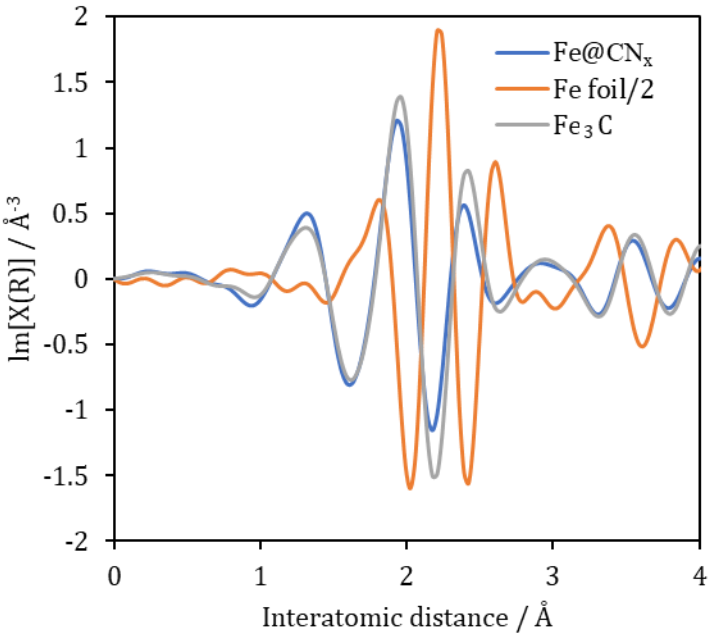


Figure S8: Imaginary part of FT-EXAFS spectra of Fe@$CN_x$ and metallic Fe foil (intensity divided by 2) and $Fe_3C$ as references. R represents interatomic distance.

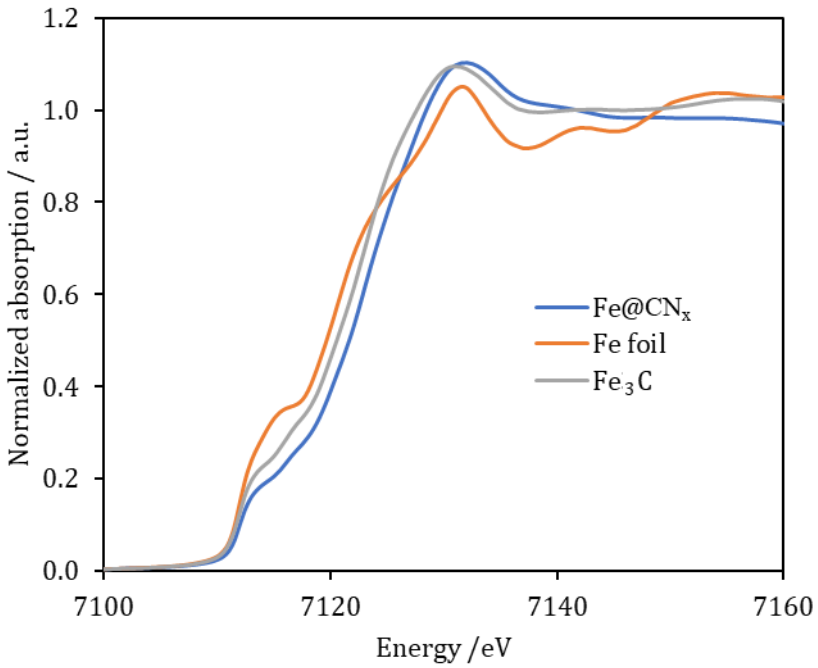


Figure S9: Comparison between the Fe K-edge XANES experimental spectrum of $Fe@CN_x$ (blue line), metallic Fe foil (orange line) and $Fe_3C$ (grey line).

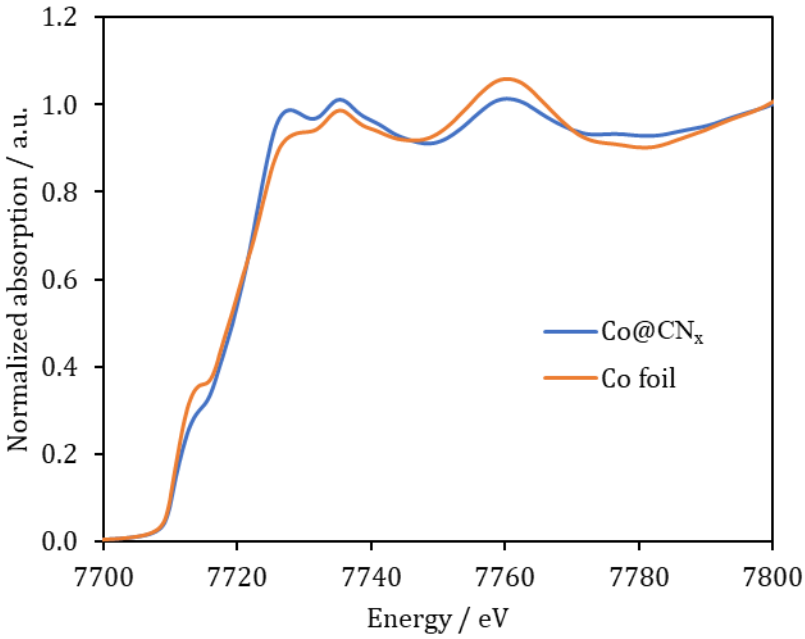


Figure S10: Comparison between the Co K-edge XANES experimental spectrum of $Co@CN_x$ (blue line) and metallic Co foil (orange line).

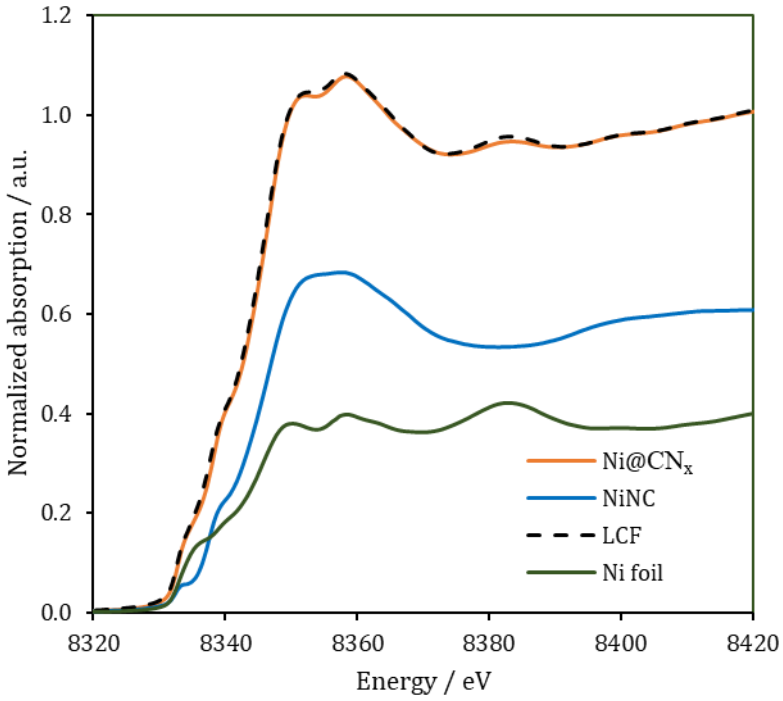


Figure S11: Linear combination fit (LCF) of the Ni K-edge XANES spectrum of Ni@$CN_x$ using Ni foil (green) and SAC NiNC (blue) as references. The orange curve represents the experimental spectrum, while the black dashed curve represents the calculated spectrum.

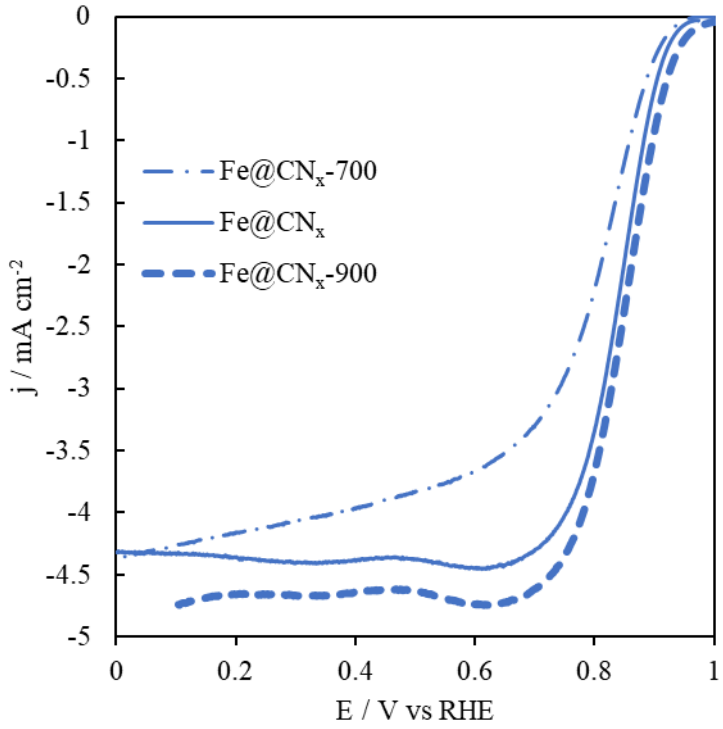


Figure S12: LSV curves of $Fe@CN_x$ samples heat-treated at 700, 800 and 900ºC in $O_2$-saturated 0.1 M KOH solution at a scan rate of 5 $mV \cdot s^{-1}$ and 1600 rpm, compared to Pt/C commercial electrocatalyst.

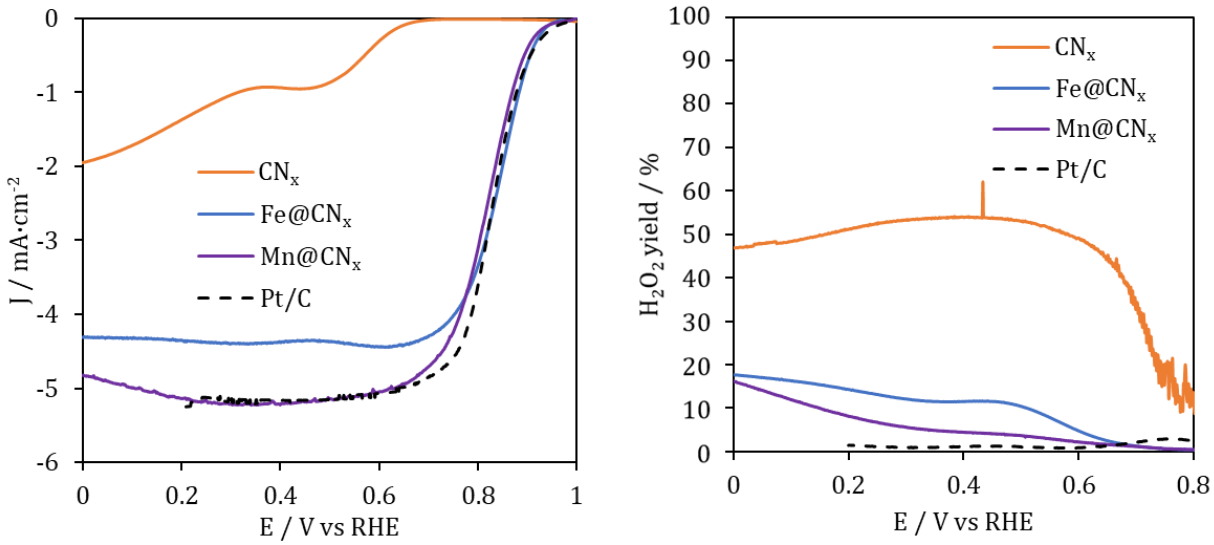


Figure S13: LSV curves (left) and hydrogen peroxide yield (right) for $Fe@CN_x$ and $Mn@CN_x$ in comparison with pristine $C_1N_1$ and commercial Pt/C electrocatalyst.

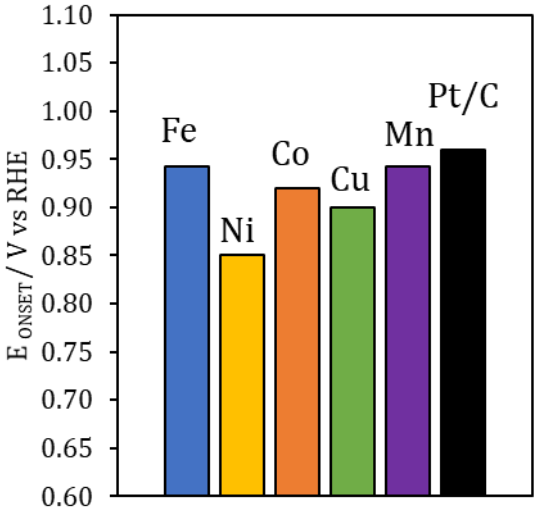


Figure S14: Schematic representation of the TM@$CN_x$ materials versus the $E_{ONSET}$ of the ORR measurements obtained from LSV curves in a $O_2$-saturated 0.1 M KOH solution.

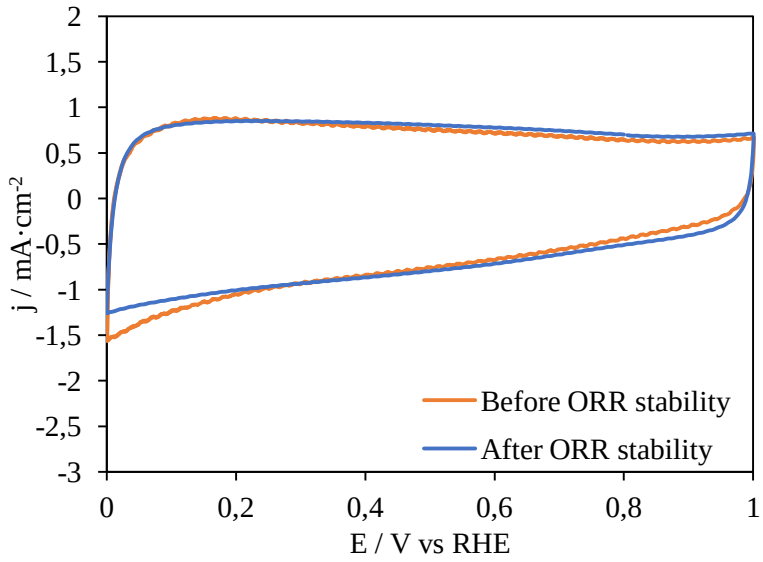


Figure S15: Cyclic voltammograms of Fe@$CN_x$ before and after the ORR stability test in a $N_2$-saturated 0.1 M KOH solution. Scan rate = 50 $mV \cdot s^{-1}$.

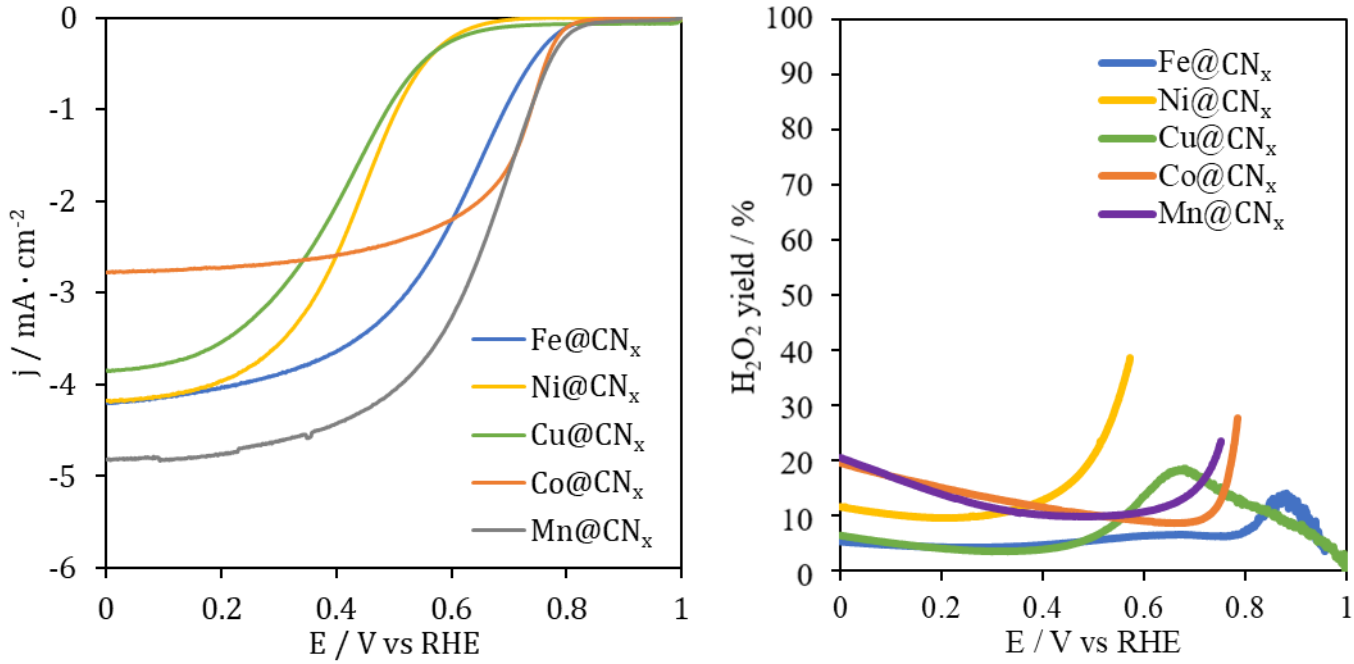


Figure S16: LSV curves (left) and hydrogen peroxide yield (right) of $TM@CN_x$ samples in $O_2$-saturated 0.5 M $H_2SO_4$ solution at a scan rate of 5 $mV \cdot s^{-1}$ and 1600 rpm.

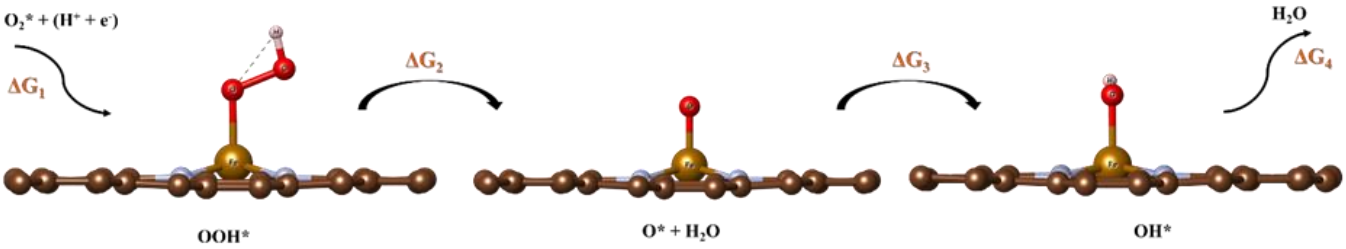


Figure S17: Elementary reaction structures of ORR on the G-$N_4$-Fe surface. The adsorbed states for the reactions include *OOH, *O and *OH species.

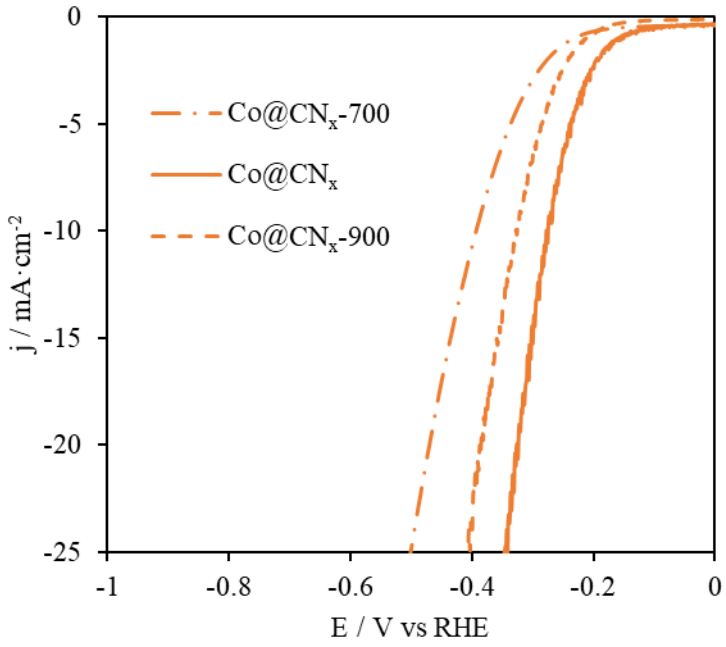


Figure S18: LSV curves of $Co@CN_x$ heat-treated at 700, 800 and 900 ºC in a $N_2$-saturated 1.0 KOH solution at a scan rate of 5 $mV \cdot s^{-1}$ and 1600 rpm.

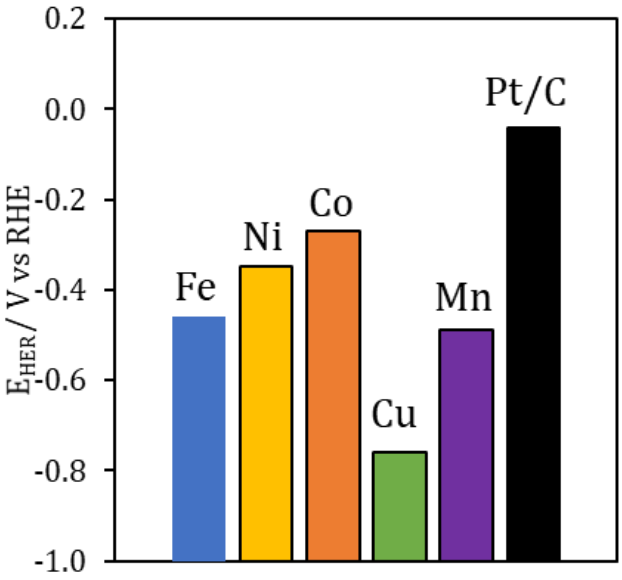


Figure S19: Schematic representation of $E_{HER}$ potential, obtained at -10 mA $cm^{-2}$, for all materials and Pt/C catalysts.

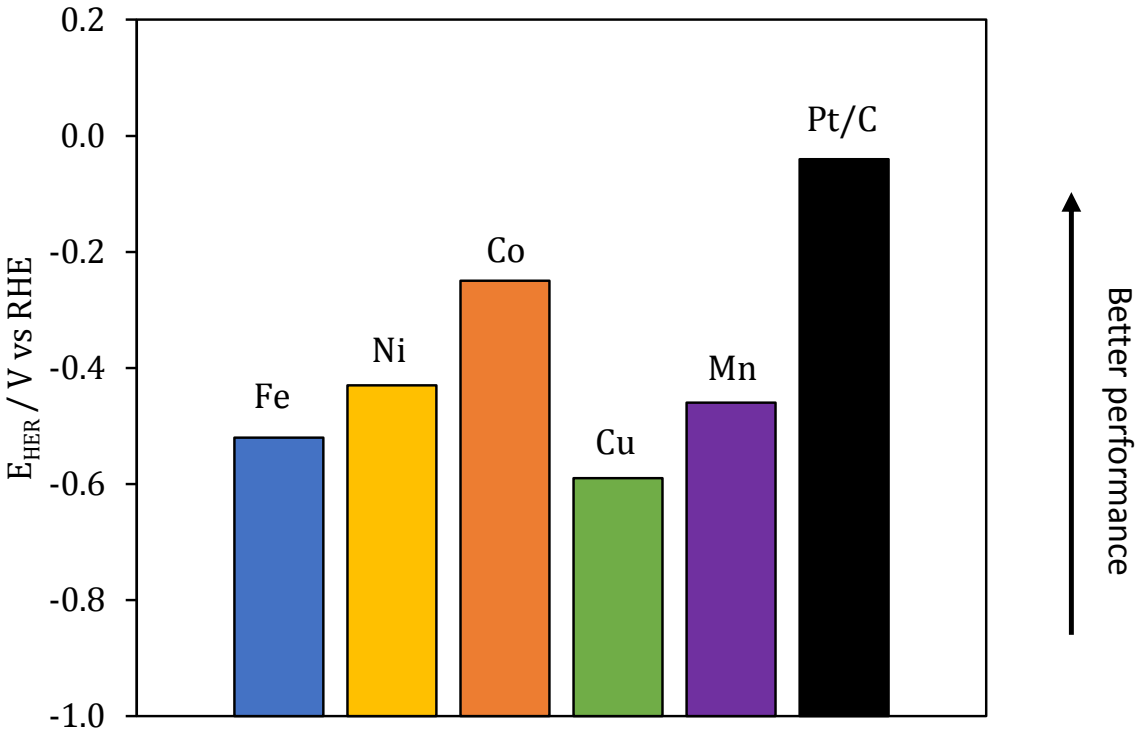


Figure S20: Schematic representation of the $E_{HER}$ potential, obtained at -10 mA·cm$^{-2}$ for all TM@CN$_x$ materials and the commercial Pt/C electrocatalyst in $N_2$-saturated 0.5 M $H_2SO_4$ solution at 5 mV·s$^{-1}$ and 1600 rpm.

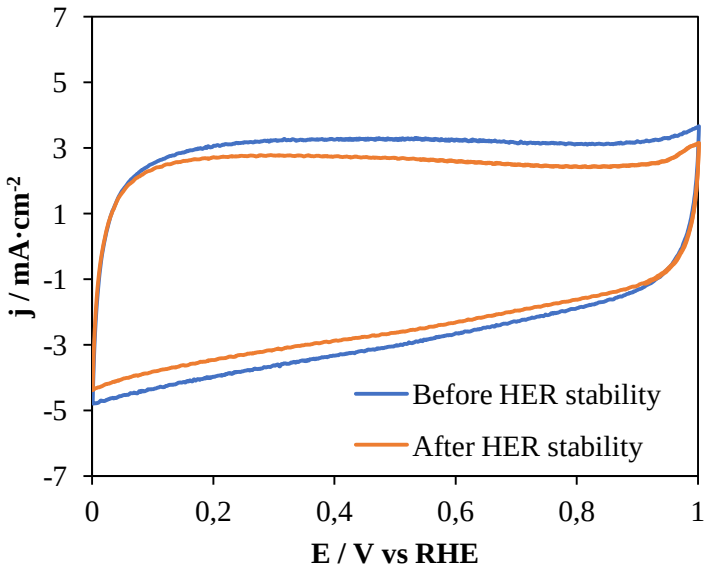


Figure S21: Cyclic voltammograms of $Co@CN_x$ before and after the HER stability test in a $N_2$-saturated 1.0 M KOH solution. Scan rate = 50 $mV \cdot s^{-1}$. The reduction in electrode current density after the stability test can be related to the partial detachment of the material under the working conditions due to the $H_2$ bubbles produced.

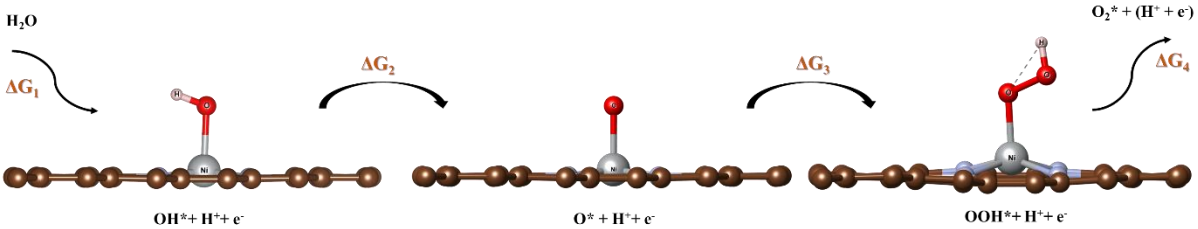


Figure S22: Elementary reaction structures of OER on the G-$N_4$-Ni surface. The adsorbed states for the reactions include *OH, *O and *OOH species.

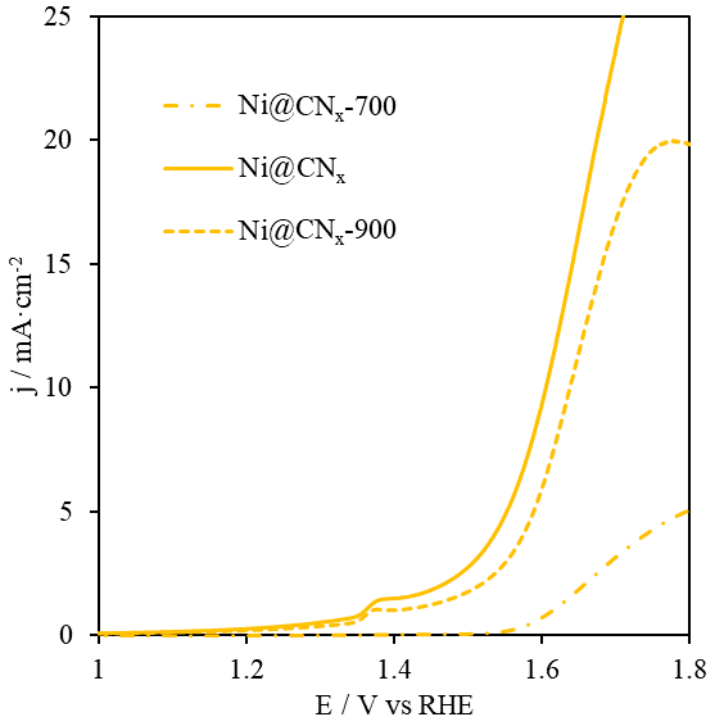


Figure S23: LSV curves of the Ni@$CN_x$ obtained at different temperatures (700, 800 and 900 ºC) in a $N_2$-saturated 1.0 KOH solution at a scan rate of 5 $mV \cdot s^{-1}$ and 1600 rpm.

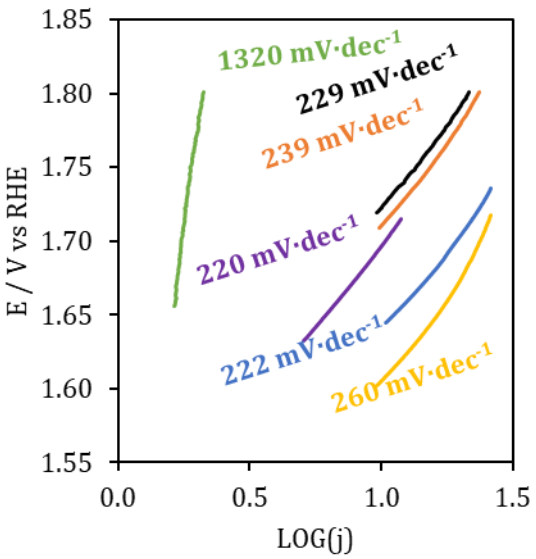


Figure S24: Tafel slopes obtained from the LSV curves of the OER for TM@$CN_x$ materials in $N_2$-saturated 1 M KOH solution at a scan rate of 5 $mV \cdot s^{-1}$ and 1600 rpm.

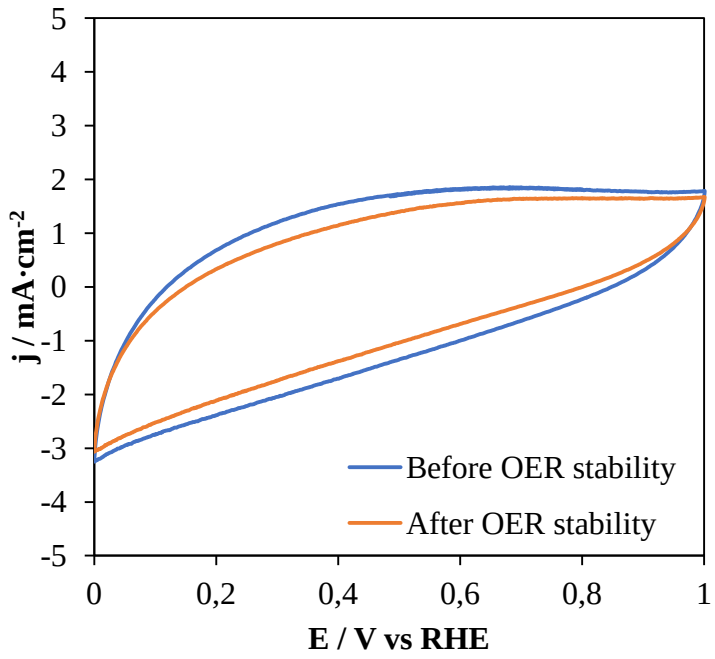


Figure S25: Cyclic voltammograms of Ni@$CN_x$ before and after the OER stability test in a $N_2$-saturated 1.0 M KOH solution. Scan rate = 50 $mV \cdot s^{-1}$. The reduction in the electrode current density after the stability test can be related to the partial detachment of the material under the working conditions due to the $O_2$ bubbles produced.

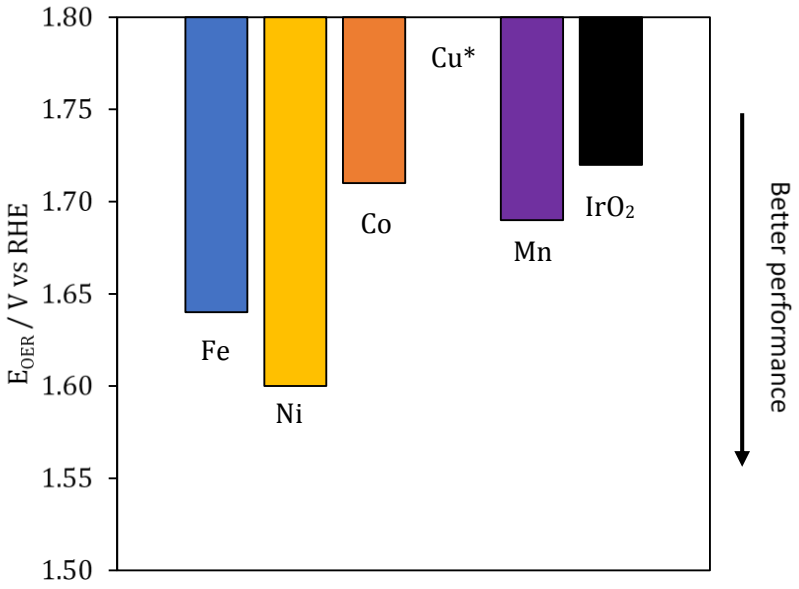


Figure S26: Schematic representation of the $E_{OER}$ potential, obtained at 10 mA·cm$^{-2}$ for all TM@CN$_x$ materials and the commercial $IrO_2$ electrocatalyst in $N_2$-saturated 1.0 M KOH solution at 5 mV·s$^{-1}$ and 1600 rpm. *Cu@CN$_x$ does not reach the $E_{OER}$ in the studied potential range.

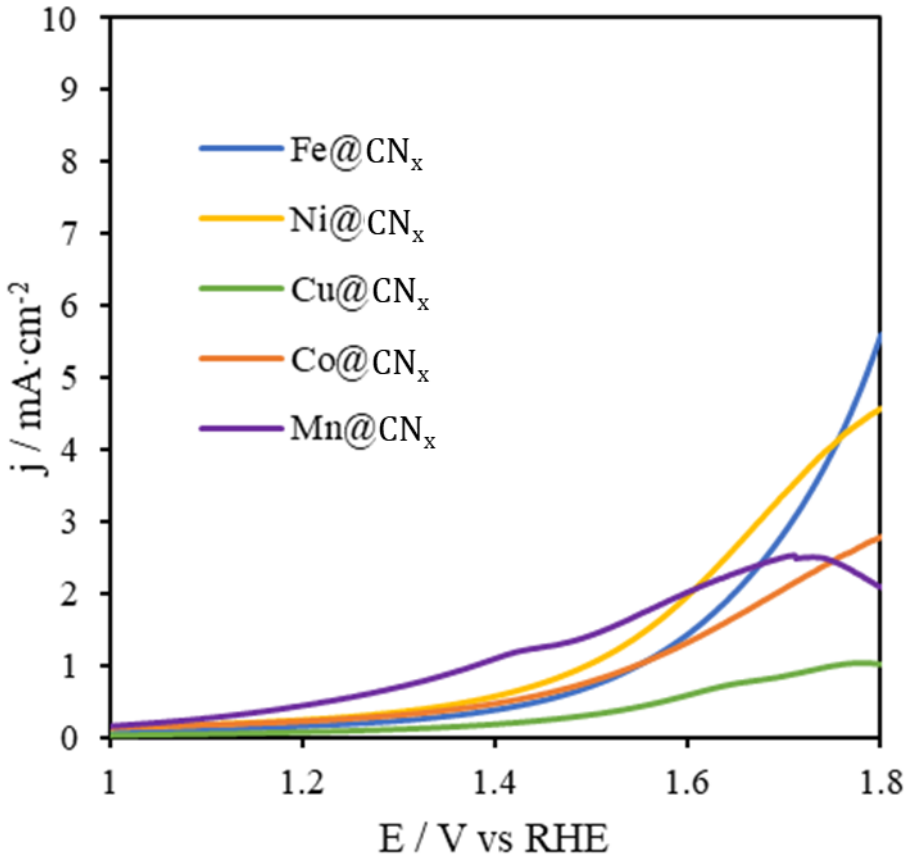


Figure S27: LSV curves for TM@$CN_x$ materials for the OER in $N_2$-saturated 0.5 M $H_2SO_4$ solution at a scan rate of 5 $mV \cdot s^{-1}$ and 1600 rpm. The $E_{OER}$ indicator is not reached because of the poor catalytic activity in the acidic electrolyte. Furthermore, some of the materials show corrosion-like profiles since the carbon structure supporting the metal active phases can be oxidized at this high potential in the presence of sulfuric acid.

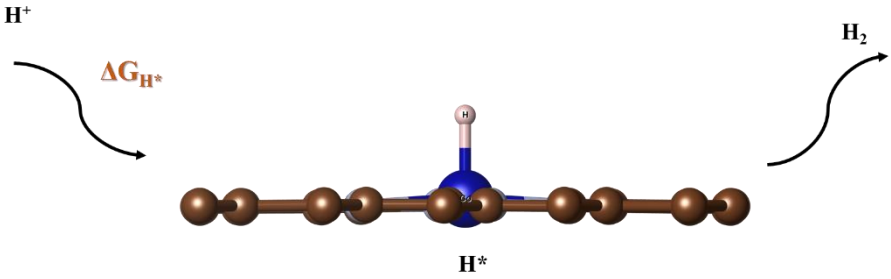


Figure S28: Elementary reaction structure of HER on the G-$N_4$-Co surface.

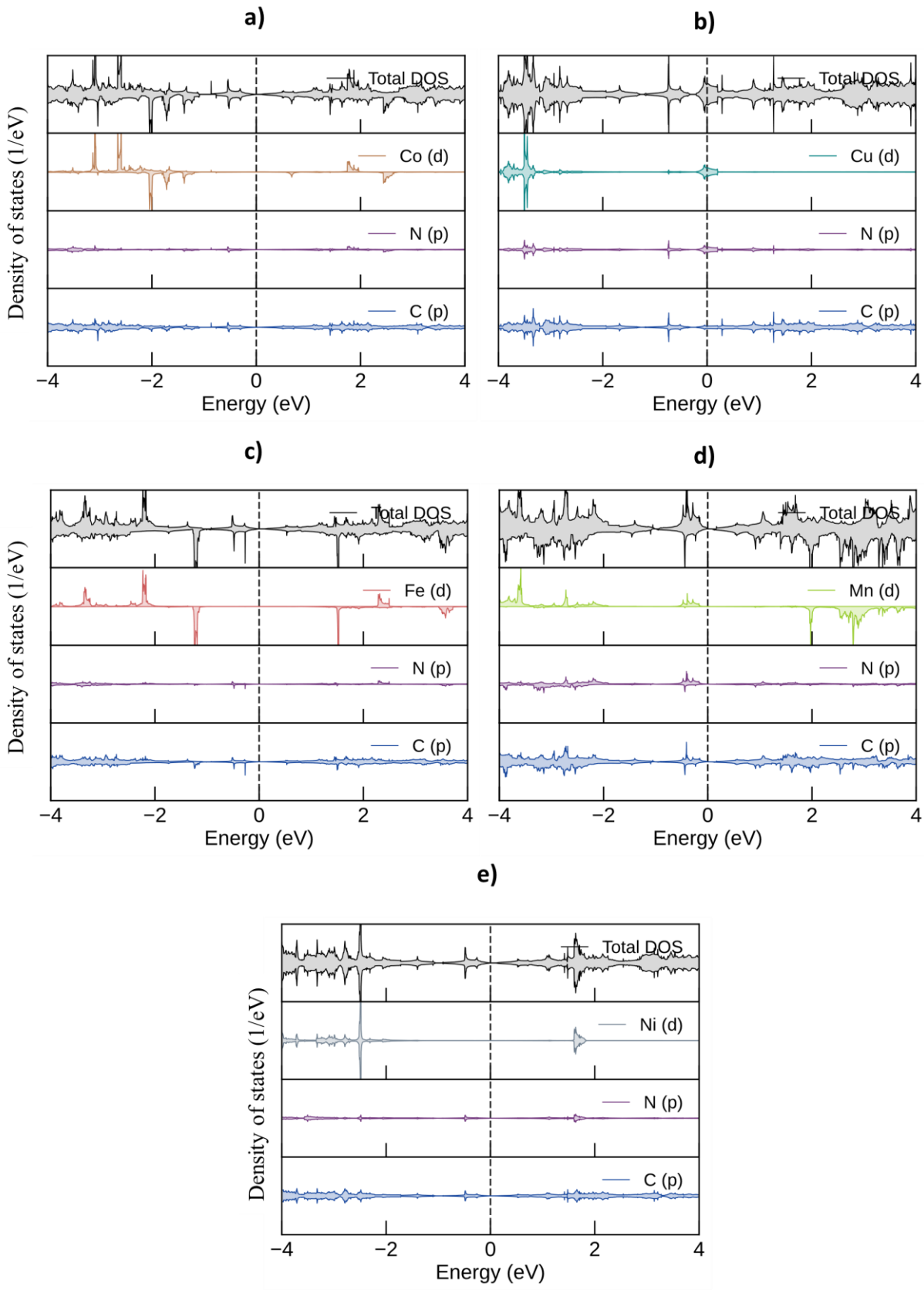


Figure S29: DOS and PDOS of pristine (a) G-$N_4$-Co, (b) G-$N_4$-Cu, (c) G-$N_4$-Fe, (d) G-$N_4$-Mn, and (e) G-$N_4$-Ni monolayers.

Table S1: Carbonization yield, metal contents (determined by ICP-MS), carbon, nitrogen, oxygen and hydrogen contents (determined by elemental analysis), and data of textural properties (from $N_2$ adsorption isotherms) of all TM@$CN_x$ materials.

| *Sample* | *Carbonization yield / %* | *Metal content / wt.%* | *Carbon content wt.%* | *Nitrogen content / wt.%* | *Oxygen content / wt.%* | *Hydrogen content / wt.%* | $S_{NLDFT}$ / $m^2\ g^{-1}$ | $V_{tot}$ / $cm^3\ g^{-1}$ | $V_{micro}$ / $cm^3\ g^{-1}$ | $V_{umicro}$ / $cm^3\ g^{-1}$ |
|---|---|---|---|---|---|---|---|---|---|---|
| $C_1N_1$ | - | - | 49.0 | 36.8 | 12.4 | 1.7 | 280 | 0.30 | 0.08 | 0.05 |
| *Fe@$CN_x$* | 40.9 | 9 | 76.7 | 2.3 | 7.8 | 0.1 | 310 | 0.54 | 0.08 | 0.02 |
| *Ni@$CN_x$* | 41.4 | 11 | 70.0 | 11.6 | 5.9 | 0.2 | 310 | 0.53 | 0.07 | 0.01 |
| *Cu@$CN_x$* | 35.2 | 14 | 52.1 | 21.6 | 11.7 | 0.3 | 230 | 0.44 | 0.06 | 0.02 |
| *Co@$CN_x$* | 41.5 | 17 | 67.9 | 7.6 | 8.7 | 0.4 | 310 | 0.54 | 0.08 | 0.02 |
| *Mn@$CN_x$* | 38.7 | 6 | 75.9 | 7.1 | 12.4 | 0.6 | 210 | 0.40 | 0.06 | 0.02 |

Table S2: Best-fit parameters obtained from the Cu and Mn K-edge EXAFS analysis of $Cu@CN_x$ and $Mn@CN_x$. $\sigma^2$ represents the Debye-Waller factor, and Coord. Nb is the coordination number. Errors are given in parentheses, e.g. 0.195(0.01) means 0.194-0.196.

| *Name* | | *Interatomic distance (nm)* | *$\sigma^2$ ($10^{-6}$ $nm^2$)* | *Coord. Nb* |
|---|---|---|---|---|
| *$Cu@CN_x$* | Cu-N(O,C) | 0.195(0.01) | 62(4) | 3.6(0.4) |
| | Cu-C | 0.312(0.02) | 250(5) | 7.3(1.0) |
| *$Mn@CN_x$* | Mn-N(O,C) | 0.203(0.03) | 93(6) | 2.5(0.8) |
| | Mn-Mn | 0.223(0.02) | 110(3) | 1.4(0.5) |

Table S3: Literature search of the best catalytic materials towards the ORR, and comparison with our own materials.

| *Metal* | *Name of the sample* | *$E_{ONSET}$ / V vs RHE* | *$E_{1/2}$ / V vs RHE* | *Reference* |
|---|---|---|---|---|
| *Fe* | $Fe@CN_x$ | 0.94 | 0.84 | This work |
| | Fe-N-CNF | 0.93 | 0.82 | S1 |
| | Fe-ISA/NC | 0.90 | 0.84 | S2 |
| *Ni* | $Ni@CN_x$ | 0.85 | 0.74 | This work |
| | Ni-SA/G-0 | 0.75 | 0.65 | S3 |
| | Ni-N4/GHSs | 0.83 | 0.72 | S4 |
| *Cu* | $Cu@CN_x$ | 0.90 | 0.79 | This work |
| | Cu1/NC-900 | 0.92 | 0.85 | S5 |
| | 0.7%Cu@NG-750 | 0.90 | 0.84 | S6 |
| *Co* | $Co@CN_x$ | 0.92 | 0.84 | This work |
| | Co-SAs@NC | 0.88 | 0.84 | S7 |
| | SACo-N/C | 0.93 | 0.88 | S8 |
| *Mn* | $Mn@CN_x$ | 0.94 | 0.84 | This work |
| | Mn/C-NO | 0.94 | 0.86 | S9 |
| | MnSAC | 0.96 | 0.88 | S10 |

Table S4: Literature search of the best catalytic materials towards the HER, and comparison with our own materials.

| *Metal* | *Name of the sample* | *Overpotential / mV* | *$E_{HER}$ / V vs RHE* | *Reference* |
|---|---|---|---|---|
| *Fe* | $Fe@CN_x$ | 460 | -0.460 | This work |
| | $Fe_2O_3$-NCs-700 | 245 | -0.245 | S19 |
| | $Fe_2O_3$-NS-C-800 | 270 | -0.270 | S20 |
| *Ni* | $Ni@CN_x$ | 350 | -0.350 | This work |
| | Ni SA/NP-NCF-800 | 138 | -0.138 | S21 |
| | Ni NP/Ni-N-C | 147 | -0.147 | S22 |
| *Cu* | $Cu@CN_x$ | 760 | -0.760 | This work |
| | Cu-CMP850 | 350 | -0.350 | S15 |
| | Cu/C | 471 | -0.471 | S23 |
| *Co* | $Co@CN_x$ | 270 | -0.270 | This work |
| | Co-N-C Mel | 196 | -0.196 | S24 |
| | Co1/CN | 138 | -0.138 | S25 |
| *Mn* | $Mn@CN_x$ | 490 | -0.49 | This work |
| | MnO@CN | 335 | -0.335 | S28 |

Table S5: Literature search of the best catalytic materials towards the OER, and comparison with our own materials.

| *Metal* | *Name of the sample* | *Overpotential / mV* | *$E_{OER}$ / V vs RHE* | *Reference* |
|---|---|---|---|---|
| *Fe* | $Fe@CN_x$ | 410 | 1.64 | This work |
| | Fe-N-C-800 | 540 | 1.77 | S11 |
| | $Fe\text{-}N_4$ SAs | 430 | 1.66 | S12 |
| *Ni* | $Ni@CN_x$ | 370 | 1.59 | This work |
| | Ni-O-G SACs | 220 | 1.45 | S13 |
| | $Ni\text{-}N_4$ SAs | 400 | 1.63 | S14 |
| *Cu* | $Cu@CN_x$ | >570* | >1.80* | This work |
| | Cu-CMP | >570* | >1.80* | S15 |
| *Co* | $Co@CN_x$ | 480 | 1.71 | This work |
| | $CoN_4$/NG | 380 | 1.61 | S16 |
| | CoSAs@CNTs | 410 | 1.64 | S17 |
| *Mn* | $Mn@CN_x$ | 460 | 1.69 | This work |
| | MnSAC | 350 | 1.58 | S10 |
| | $MnO_x$/S-GC | 390 | 1.62 | S18 |

* The $E_{OER}$ value was not reached in the OER experiments

Table S6: Bond lengths (d), Magnetic moment (m), Metal atom out-of-plane dislocation (Δz), and electronic energy of G-$N_4$-TM in different spin states.

| ***System*** | ***$d_{M-N}$ (Å)*** | ***$d_{N-C}$ (Å)*** | ***Δz (Å)*** | ***m (μB)*** | ***E (eV)*** |
|---|---|---|---|---|---|
| *G–$N_4$–Fe* | 1.87 | 1.36 | 0.04 | 0.00 | -280.25 |
| | **1.88** | **1.36** | **0.04** | **2.00** | **-280.74** |
| | 1.98 | 1.36 | 0.49 | 4.00 | -280.00 |
| *G–$N_4$–Ni* | **1.86** | **1.36** | **0.00** | **0.00** | **-277.73** |
| | 1.89 | 1.35 | 0.00 | 2.00 | -277.00 |
| *G–$N_4$–Co* | **1.86** | **1.36** | **0.00** | **1.00** | **-280.16** |
| | 1.95 | 1.35 | 0.43 | 3.00 | -278.95 |

Table S7: Adsorption energy ($E_{ads}$), Bond lengths (d), Magnetic moment (m), Fe atom out-of-plane dislocation (Δz), and Multiplicity of $O_2$ adsorbed on G-$N_4$-Fe in different configurations. Insets: Geometric representation of a) end-on and b) side-on.

| *System* | *Geometry* | $E_{ads}$ *(eV)* | $d_{O–O}$ *(Å)* | $d_{M–O}$ *(Å)* | *Δz (Å)* | *m (μB)* | *Multiplicity* |
|---|---|---|---|---|---|---|---|
| *G–Fe–$N_4$:$O_2$* | Side-on | -1.09 | 1.37 | 1.88 / 1.88 | 0.54 | 0 | 1 |
| | Side-on | -1.55 | 1.39 | 1.87 / 1.87 | 0.74 | 2 | 3 |
| | Side-on | -1.60 | 1.32 | 2.16 / 2.16 | 0.53 | 4 | 5 |
| | End-on | -1.19 | 1.30 | 1.72 | 0.48 | 0 | 1 |
| | End-on | -1.63 | 1.30 | 1.89 | 0.43 | 2 | 3 |
| | End-on | -1.47 | 1.26 | 2.46 | 0.15 | 4 | 5 |

a)

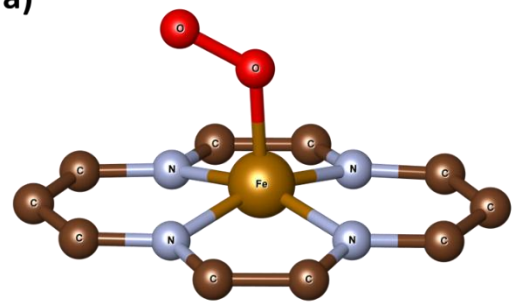


b)

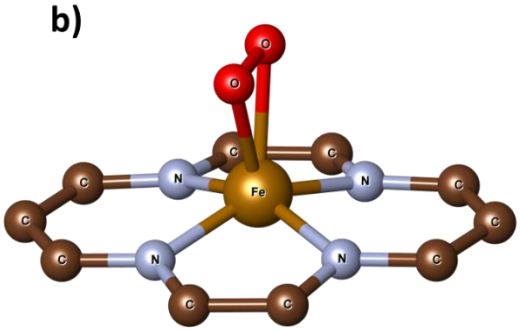

**References**

S1 Z.Y. Wu, X.X. Xu, B. C. Hu, H.W. Liang, Y. Lin, L.F. Chen, S.H. Yu, Angew. Chem. Int. Ed. 2015, 54, 8179-8183.
S2 Q. Li, W. Chen, H. Xiao, Y. Gong, Z. Li, L. Zheng, X. Zheng, W. Yan, W.C. Cheong, R. Shen, N. Fu, L. Gu, Z. Zhuang, C. Chen, D. Wang, Q. Peng, J. Li, Y. Li, Adv. Mater. 2018, 30, 1800588.
S3 X. Song, N. Li, H. Zhang, L. Wang, Y. Yan, H. Wang, L. Wang, Z. Bian, ACS Appl. Mater. Interfaces, 2020, 12, 15.
S4 J. Chen, H. Li, C. Fan, Q. Meng, Y. Tang, X. Qiu, G. Fu, T. Ma, Adv. Mater. 2020, 32, 2003134.
S5 W. Wu, Y. Liu, D. Liu, W. Chen, Z. Song, X. Wang, Y. Zheng, N. Lu, C. Wang, J. Mao, Y. Li, Nano Research, 2021, 14, 998-1003.
S6 L. Bai, C. Hou, X. Wen, J. Guan, ACS Appl. Energy Mater. 2019, 2, 4755-4762.
S7 C. Shi, Y. Liu, R. Qi, J. Li, J. Zhu, R. Yu, S. Li, X. Hong, J. Wu, S. Xi, L. Zhou, L. Mai, Nano Energy, 2021, 87, 106153.
S8 Y. Wang, L. Chen, Z. Mao, L. Peng, R. Xiang, X. Tang, J. Deng, Z. Wie, Q. Liao, Sci. Bull. 2019, 64, 1095-1102.
S9 Y. Yang, K. Mao, S. Gao, H. Huang, G. Xia, Z. Lin, P. Jiang, C. Wang, H. Wang, Q. Chen., Adv. Mater. 2018, 30, 1801732.
S10 H. Shang, W. Sun, R. Sui, J. Pei, L. Zheng, J. Dong, Z. Jiang, D. Zhou, Z. Zhuang, W. Chen, J. Zhang, D. Wang, Y. Li, Nano Lett. 2020, 20, 5443-5450.
S11 J. Xu, L. Shi, C. Liang, H. Wu, J. Lei, D. Liu, D. Qu, Z. Xie, J. Li, H. Tang, ChemElectroChem 2017, 4, 1148-1153.
S12 Y. Pan, S. Liu, K. Sun, X. Chen, B. Wang, K. Wu, X. Cao, W.C. Cheong, R. Shen, A. Han, Z. Chen, L. Zheng, J. Luo, Y. Lin, D. Wang, W. Peng, Q. Zhang, C. Chen, Y. Li, Angew. Chem. Int. Ed. 2018, 57, 8614-8618.
S13 Y. Li, Z.S. Wu, P. Lu, X. Wang, W. Liu, Z. Liu, J. Ma, W. Ren, Z. Jiang, X. Bao, Adv. Sci. 2020, 7, 1903089.
S14 J. Chen, H. Li, C. Fan, Q. Meng, Y. Tang, X. Qiu, G. Fu, T. Ma, Adv. Mater. 2020, 32, 2003134.
S15 S. Cui, M. Qian, X. Liu, Z. Sun, P. Du, ChemSusChem 2016, 9, 2365-2373.
S16 L. Yang, L. Shi, D. Wang, Y. Lv, D. Cao, Nano Energy 2018, 50, 691-698.
S17 S. Dilpazir, H. He, Z. Li, M. Wang, P. Lu, R. Liu, Z. Xie, D. Gao, G. Zhang, ACS Appl. Energy Mater. 2018, 1, 3283-3291.
S18 Y. Gao, H. Zhao, D. Chen, C. Chen, F. Ciucci, Carbon 2015, 94, 1028-1036.
S19 J. Jiang, L. Zhu, Y. Sun, Y. Chen, H. Chen, S. Han, H. Lin, J. Power Sources 2019, 426, 74-83.
S20 S. Chao, Q. Xia, G. Wang, X. Zhang, Int. J. Hydrog. Energy 2019, 44, 4707-4715.
S21 J. Yu, J. Li, C.Y. Xu, Q. Liu, J. Liu, R. Chen, J. Zhu, R. Li, J. Wang, Carbon 2021, 185, 96-104.
S22 C. Lei, Y. Wang, Y. Hou, P. Liu, J. Yang, T. Zhang, X. Zhuang, M. Chen, B. Yang, L. Lei, C. Yuan, M. Qiy, X. Feng, Energy Environ. Sci. 2019, 12, 149-156.
S23 M.A. Ahsan, A.R.P. Santiago, Y. Hong, N. Zhang, M. Cano, E. Rodriguez-Castellon, L. Echegoyen, S.T. Sreenivasan, J.C. Noveron, J. Am. Chem. Soc. 2020, 142, 14688-14701.
S24 S. Li, Q. Zhou, G. Yu, Z. Lei, Z. Liu, Q. Xu, W. Xu, R. Wu, Appl. Surf. Sci. 2020, 518, 146239.
S25 L. Cao, Q. Luo, W. Liu, Y. Lin, X. Liu, Y. Cao, W. Zhang, Y. Wu, J. Yang, T. Yao, S. Wei, Nat. Catalysis 2019, 2, 134-141.

S28 J. li, Y. Wang, T. Zhou, H. Zhang, X. Sun, J. Tang, L. Zhang, A.M. Al-Enizi, Z. Yang, G. ZhengJ. Am. Chem. Soc. 2015, 137, 14305-14312.